Eindhoven University of Technology
Department of Applied Physics
Graduate school
MSc Applied Physics (Nano, Quantum and Photonics)

Light Induced Damage of Silicon Nitride with femtosecond laser

Internship report

Author: J. Lopez Leyva 1330594

Supervisors:
ARCNL: Prof.dr.Paul Planken (external supervisor) (Light Matter Interaction)
ARCNL: MSc.Ester Abram (daily PhD supervisor) (Light Matter Interaction)
ASML: Dr.Vina Faramarzi (2_{nd} external supervisor) (Light-induced damage in materials)
TU/e: Prof.dr.Jaime Gómez Rivas (AP supervisor) (Photonics and Semiconductor Nanophysics)
TU/e: Prof.dr.Adriana Creatore (2_{nd} AP supervisor) (Plasma & Materials Processing)

University of Eindhoven
September, 2023

1 Abstract

This report focuses on studying optical damage of thin Silicon Nitride (20nm) on Silicon (bulk), and Silicon Nitride (120nm) on Silicon Dioxide (18nm) on Silicon (bulk). These samples are damaged with a 45fs single pulse at 400nm central wavelength (pump) and measured with a 45fs 800nm central wavelength (probe) in a pump-probe setup.

For the Silicon Nitride on Silicon sample, it's found that for pulses below the ablation threshold, there's likely a crystal/amorphous phase change underneath the Silicon Nitride layer (Silicon or Silicon native oxide). For pulses near the ablation threshold, complete delamination is observed for the Silicon Nitride on Silicon sample. Aditonally, microstructural changes at the center of delamination and at the parts where Silicon Nitride is not yet delaminated is seen with SEM and AFM. For pulses above the ablation threshold, multiple damage regimes with different morphology are identified. In these regimes, Silicon removal is observed with "pit" morphology, as well as planar delamination.

For the Silicon Nitride on Silicon Dioxide on Silicon sample, similar behavior as for the Silicon Nitride on Silicon sample is found for pulses below the ablation threshold. Meaning, a phase change is observed. However, not only the phase of the buried silicon but the silicon nitrate itself can change. For Pulses near the ablation threshold, morphology of bulging and "donuts" (circular areas where height increases at the edges) are observed. For pulses above the ablation threshold, cascading craters are seen. The thickness of these craters suggest that damage in Si substrate does not play a dominant role (compared to other possible mechanisms) due to Silicon Nitride not being removed from the Silicon substrate upwards.

Contents

2 Introduction

2.1 Literature review

2.1.1 Background of the work

The reason for studying Light Induced damage (LID) of Silicon Nitride (Si_yN_x) is its relevance in photonics [1–4], solar [5–8] and the semiconductor/electronics industry [9–15]. Specifically, Si_yN_x is used as low loss photonic waveguides for light and acoustics. For photonics, it exhibits a wide bandgap, low losses and low non-linear absorption coefficient at telecom wavelengths. For solar, it acts as a anti-reflection coating in solar panels and a passivation layer. A passivation layer protects a surface (typically semiconductor) from chemical and electrical instabilities, and offers mechanical protection and insulation from metal traces. In semiconductors, it acts mainly as a passivisation layer in Back End Of Line (BEOL) and Front End Of Line (FEOL) of a microchip.

Thus, due to the wide array of applications, understanding damage mechanisms such as ablation is of high importance. The damage risks for $SiyN_x$ are reported to be due to two-photon-absorption and heat transfer due to multilayer stacks [16]. For instance, in the case of ASML's nanolithography, laser powers must be controlled such that unwanted Si_yN_x (or other materials) ablation doesn't occur on chips. On the other hand, controlled ablation can also be used for patterning Si_yN_x strucutures with femtosecond lasers [17, 18].

Previous work in this field provides multiple results on damage of Si_yN_x on Si with femtosecond lasers of 660+ fs pulse duration, 1053nm wavelength and 20-84µm beam spot FWHM. [19–21]. However, a key difference from this report is the setup, where a wavelength of 400nm, pulse duration of 45fs, and beam spot of 75-120µm is used instead. This is an important remark, since literature on Si ablation shows different behavior for shorter pulse durations of 20-200fs, varying from Coulomb Explosion, plasma formation, phase change to micro particle ejection [22–29]. The results found in this report, seem to match those found for shorter pulse durations (Si literature), giving indications of morphology (microstructural changes) reffered to as NanoHill(Locks) [22] or surface texturing [23]. The report will refer to them as microstructural changes. This shows an interesting yet unexplored regime of Si_yN_x ablation science, which will be covered in this report.

2.1.2 Research objectives and method

- Characterize ablation of Si-Si_yN_x(20nm)
- Characterize ablation of Si-SiO_2(20nm)-Si_yN_x(120nm)
- Compare ablation mechanisms to literature

The studied stacks are Silicon - Silicon Nitride (Si-Si_yN_x) with 20nm of Si_yN_x, as well as Silicon - Silicon Dioxide -Silicon Nitride (Si-SiO_2-Si_yN_x) stack with Si_yN_x thickness of 120nm and SiO_2 thickness of 20nm. The Si-Si_yN_x thicknesses are chosen because these are thinner than literature and of interest to ASML. The Si-SiO_2-Si_yN_x thicknesses are chosen because this multilayer configuration is common in the photonics industry, and can be directly compared to previous literature without SiO_2 layer [19–21].

To research the damage mechanisms of the thin films, experiments and simulations are done. The experiments use a femtosecond laser with varying fluence. Ablation is characterized with methods described in 4, such as a novel approach to reflectance microscopy, Atomic Force Microscopy (AFM), Scanning Electron Micoscopy (SEM) and Liu anlysis. As for simulations, these are based on multilayer matrix transfer method 5.6. (Due to time constrait, focus is placed on Si-Si_yN_x sample)

3 Theory

3.1 Definitions

Before addressing Liu analysis, it's important to define parameters used as literature does not consistently use the definitions. In this report, pulses are assumed to be spatially elliptical, and Gaussian in space and time, and 2D fluence is defined as

$$F = \frac{E}{A_{FWHM}} = F_0 exp(-\frac{R_x^2}{a^2}) exp(-\frac{R_y^2}{b^2}), \tag{1}$$

where F is the fluence, E is the total energy deposited per pulse (not limited to energy in Full Width Half Maxima area A_{FWHM}). A_{FWHM} is the Full Width Half Maxima (FWHM) area of incident Gaussian laser fluence, F_0 is the peak fluence (top fluence of Gaussian), R_x, R_y are the spatial radius, a, b are the standard Gaussian parameters. The exact method of how energy is obtained from power is explained in section 4.1.1. However, a,b are not immediately measurable parameters, so they will be simplified. Firstly, the 2D Gaussian is separated into two 1D (major and minor axis). Assuming the peak fluence overlaps (not A_{FWHM}) for major and minor axis at the center, fluence can be seprated into

$$\frac{F_0}{2} = F_0 exp(-\frac{R_x^2}{a^2}) \qquad \frac{F_0}{2} = F_0 exp(-\frac{R_y^2}{b^2}). \tag{2}$$

Since R_x, R_y are now sovled for FWHM radius, these need to be multiplied by 2 to give FWHM for major and minor axis as $\sigma_{x,y} = 2R_{x,y}$. This results in $a = \frac{\sigma_x}{2\sqrt{ln(2)}}$ and $b = \frac{\sigma_y}{2\sqrt{ln(2)}}$. These can then be reinserted into the fluence definition equation 1, giving

$$F = F_0 exp(-\frac{R_x^2 4ln(2)}{\sigma_x^2}) exp(-\frac{R_y^2 4ln(2)}{\sigma_y^2}). \tag{3}$$

Having obtained a measurable fluence, now the energy can be solved as

$$E = F_0 \iint_\infty exp(-\frac{R_x^2 4ln(2)}{\sigma_x^2}) exp(-\frac{R_y^2 4ln(2)}{\sigma_y^2}) dxdy = F_0 \sqrt{\frac{\pi\sigma_x^2}{4ln(2)}} \sqrt{\frac{\pi\sigma_x^2}{4ln(2)}} = \frac{F_0 \pi \sigma_x \sigma_y}{4ln(2)} = \frac{F_0 A_{FWHM}}{ln(2)}. \tag{4}$$

Firstly, the integral is solved with the standard Gaussian integral $\int_\infty exp(-a(x+b)^2)dx = \sqrt{\frac{\pi}{a}}$. In the last step, the definition of ellipse area is used as $A_{FWHM} = \frac{\pi\sigma_x\sigma_y}{4}$, where radius was changed to diameter (hence factor $\frac{1}{4}$). The end result for fluence is

$$F = \frac{F_0}{ln(2)} \tag{5}$$

3.2 Liu Analysis

Liu analysis (also referred to as D^2 method), is a common method used for determining the ablation threshold due to light induced damage [30]. It's based relating the size of an ablation spot to the respective fluence. Using the expression obtained in equation 3, it can be rewritten to account for an ablation threshold F_{abl} as

$$\frac{1}{4ln(2)} ln(F_0) - ln(F_{abl}) = \frac{R_x^2}{\sigma_x^2} + \frac{R_y^2}{\sigma_y^2}. \tag{6}$$

Since x and y directions are assumed to be independent, the equation can be solved via parametrization (e.g. set $R_y = 0$, then solve for x direction). Meaning that the problem simplifies to two 1D problems again, resulting in

$$\frac{\sigma_{x,y}^2}{4ln(2)} ln(F_0) - ln(F_{abl}) = R_{x,y}^2, \tag{7}$$

where both expressions are given for x or y. Knowing the area of an ellipse $A = \pi R_x R_y$, the results for R_x and R_y can be multiplied to give an area as

$$\frac{\sigma_x \sigma_y}{4ln(2)} ln(F_0) - ln(F_{abl}) = A, \tag{8}$$

which can be written as linear (logarithmic) regression as

$$A = \alpha ln(F_0) + \beta \tag{9}$$

where $\alpha = \frac{\sigma_x \sigma_y}{4ln(2)}$ and $\beta = \frac{\sigma_x \sigma_y}{4ln(2)} ln(F_{abl})$ and ablation threshold is calculated as

$$F_{abl} = exp(-\frac{\beta}{\alpha}) \tag{10}$$

4 Experimental Methods

4.1 Experimental Setup

Ablation measurements are done using a pump-probe setup as depicted in figure 1 and is greatly based on the work of Abram.E [31]. The purpose of the setup is to irradiate a sample for different fluences. The fluences range from 0 to $4\frac{J}{cm^2}$ with a pulse duration of 45fs. As for the beam shape and size, the pump beam has a nearly Gaussian shape (slightly elliptical) with approximately 75µm Full Width Half Maxima (FWHM) for the Si-Si$_y$N$_x$ sample, and approximately 120µm FWHM for Si-SiO$_2$-Si$_y$N$_x$ sample. However, Si-Si$_y$N$_x$ sample has a bad beam shape, resulting in 2 ellipses at the top and bottom of the center. This is not the case for Si-SiO$_2$-Si$_y$N$_x$ sample.

As for the probe beam, the size is 15µm FWHM. This is verified with a beam profiler (Gentec-EO Beamage-4M) before starting to measure the sample. The pump spots are separated by 200µm (this means that there is some overlap in beams spots for Si-SiO$_2$-Si$_y$N$_x$ sample due to 120µm spot size). For the varying fluences, these are made in 36 increments. Those 36 fluences form a grid of 6 rows and 6 columns (increasing fluence left to right, top to bottom) as seen in figure 4. Multiple grids are made on the same sample.

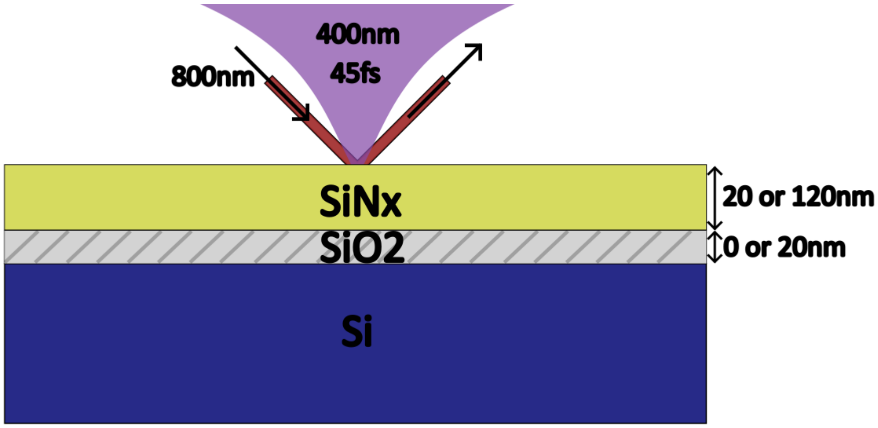

Figure 1: Diagram pump-probe experiment. Three materials can be seen, where Si is the substrate, SiO$_2$ can have thickness of 0 (only native Si oxide) or 20nm, and Si$_y$N$_x$ can be 20 or 120nm. Exact composition of Si-SiN$_x$ and Si-SiO$_2$-Si$_y$N$_x$ samples are listed in table 4.3.5. The purple cone represents the pump laser beam with a central wavelength of 400nm (50nm FWHM) and pulse duration of 45fs. The red beams represent the probe laser at 800nm central wavelength with a smaller beam spot than the probe beam

Full setup is shown in figure 2. Firstly, a Ti:Sapphire generates a 45fs laser at 800nm central wavelength with a repetition rate of 1KHz. This is then split via a 99/1 beam splitter, such that a strong pump and weak probe signal are splitted. The pulse then passes through a half wavelength plate, which is mounted on a piezoelectric rotating stage to vary the polarization incident on the Beta Barium Borate (BBO) crystal due to Second Harmonic Generation (where pahse matching is needed), and thus control the output fluence out of the BBO. The BBO crystal upconverts the 800nm pump signal into a 400nm central wavelentgh pulse. Afterwards, the pump passes again through a half wavelength plate.

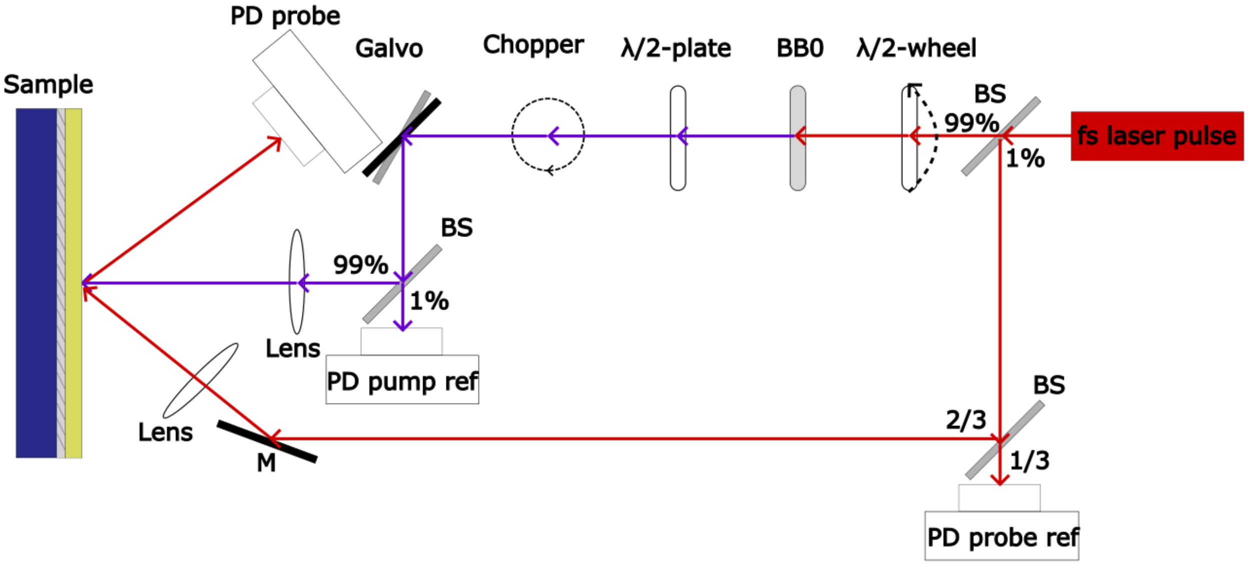

Figure 2: Setup of pump probe experiment. "BS" = Beam Splitter, "PD" = Photodetector, "ref" = reference, "M" = mirror. Red lines indicate the path of the probe beam (800nm), and blue lines the path of pump beam (400nm). Laser generation setup is not shown.

Next, it passes through a 10% duty-free chopper, reducing the frequency to 100Hz. This frequency allows the upcoming Galvo mirror to pass single pulses. Lenses are used to control beam size. The angle of incidence of the pump is normal incidence 0°, the probe has 10°. For measurements, the sample is moved in plane (XY) to a different position for each fluence. To detect the variation in pump/probe signals, 3 switchable-gain Si photodiode detectors are used (Thorlabs PDA100A2). These photodiodes are used for for obtaining reflectances and for calibration.

4.1.1 Calibration

For calibration, a coherent thermopile power sensor is placed in the pump beam path before the focusing lens. This calibrates the reference photodetector and allows conversion from photodiode to pump fluence. This is necessary because the photodetectors can saturate, and this needs to be accounted for.

In the setup and calibration, single pulse energies are used. This means that power needs to be converted to energy accordingly since 1000 pulses are measured, such that $E = \frac{power_{total}\tau}{f}$, where $power_{total}$ is the total power measured by the photodetector (after converting voltage to power).

4.2 fabrication

The thin films of Si-SiO$_2$-Si$_y$N$_x$ and Si-Si$_y$N$_x$ are grown on top of a pre-cut Si substrate of 12x12mm. The Si substrate is lightly p-doped with a resistivity of 5 to 10 Ωcm (or $1.5 * 10^{15}$-$3 * 10^{15}$ cm^{-3}). To remove contaminants, Si is cleaned via an ultra-sound bath. To do so, Si is first submerged in acetone, which is then placed inside the ultra-sound water bath for 10 minutes. Afterwards, the same is repeated with isopropanol instead of acetone. For the Si-Si$_y$N$_x$ sample, ultra-sound was also done after damage measurement, where the process is repeated, but instead of acetone, distillated water is used. The reason for cleaning again, is to remove the presence of microparticles formed during ablation which might reduce characterization accuracy. After cleaning, the Si substrates are inserted into a Inductively Coupled Plasma Chemical Vapor Deposition (ICPCVD) machine.

For the Si-SiO$_2$-Si$_y$N$_x$ sample, first a 20nm SiO$_2$ layer is grown on top of a Si substrate. The recipe is O2 (32 sccm) and SiH4 (26 sccm) at 150$^{\circ}C$, resulting in a growth rate of 90nm/min. Afterwards, for both Si-SiO$_2$-SiN$_x$ (now with 20nm SiO$_2$ grown) and Si-Si$_y$N$_x$ (without SiO$_2$, but with native Si oxide), Si$_y$N$_x$ is grown. This is done at with N2 (25sccm) and SiH4 (28sccm) at 150$^{\circ}C$, resulting in a growth rate of 43.3nm/min. The Stoichiometry is not know beforehand, but can be estimated with previous literature

(MSc thesis), giving a Silicon rich $\frac{N2}{Si} \approx 0.75$ equivalent to Si4N3 [32]. This is determined by comparing ellipsometry results obtained in A-24, specifically the n and k of Si_yN_x. This also indicate a bandgap at 400nm or 3.1eV.

4.3 Characterization

4.3.1 Reflectance Microscope

To study ablation, the reflection spectra is obtained with an Filmetrics F40 microscope. The beam spot of the reflectance microscope is 30µm, and is focused at the center of the ablation spots. For calibration, the standard Si sample provided by Filmetrics is used, and integration time of 251ms is used. Each spot each spot where the laser is incident is measured, gives an evolution of spectra as a function of fluence at the center of the ablation spot.

4.3.2 Dark Field and Bright Field Microscopy

The Dark and Bright Field microscope used is a "ZEISS Axioscope" for Materials. Images are taken at the center of the grid 10x zoom, and the Dark Field ones are also used for Liu analysis as discussed in the results section 3.

4.3.3 Atomic Force Microscopy

The Atomic Force Microscopy (AFM) used is "Dimension Icon" AFM, where "RTESPA-300" pyramidal tips from Bruker are used. Tapping mode in air is maintained through all measurements.

4.3.4 Scanning Electron Microscopy

The Scanning Electron Microscopy (SEM) used is "FEI Helios 600 DualBeam". A High Voltage (HV) of 5kV is used, with a Working Distance (WD) of 4.2mm, varying Horizontal Field View (HFW) and Magnification (mag), in scanning electron mode (SE), with a Everhart–Thornley detector (ETD), and varying tilt.

4.3.5 Ellipsometry

The Ellipsometer used is "Ellipsometer VB-400 J.A. Woollam". It's used to obtain the exact thickness of the the grown samples, as well as the refractive indices of each layer (including native oxides, layer diffusion and roughness). These results are then implemented into the simulations to increase accuracy, and also allowed to determine the stoichiometry of the grown Si_yN_x [32]. Table 4.3.5 shows the exact thickness and composition of both samples. The Mean Square Error (MSE) for Si-Si_yN_x ellipsometry data is $2.5nm^2$, for Si-SiO_2-Si_yN_x it's $2.8nm^2$

Thickness (nm)	Si-SiN	Si-SiO_2-SiN
SiN_x	21.5	121.3
Intermix	0.5	0.5
SiO_2	-	18.6
Intermix	-	0.5
Si native oxide	2	2
Si	Substrate	Substrate
(Roughness)	4.5	4.5

Table 1: Thicknesses of Si-SiN_x and Si-SiO_2-SiN_x samples. SiO_2 intermixing is not present in Si-SiN_x sample as indicated with a dash "-". Intermix represents the diffusion between layers (layers above and below intermix row in table). Roughness indicates at the outer SiN_x layer, how high surface imperfections are with the assumption that 50% of the material is air.

4.3.6 Profilometer

The Profilometer used is "KLA Tencor Stylus Profiler P7". Tip is 2µm with 60° cone radius of angled tip. The speed used is 2 µm/s at 1000Hz acquisition rate. The purpose is to obtain a rough surface morphology to obtain regions of interest, and the measurements which couldn't be measured with AFM/SEM due to time are listed in the A.

5 Results

I this report, Ablation is defined as morphological modification visible in Dark Field Microscopy. Damage is defined as any change (including ablation) where material change can be measured. If a spot number is not specified, it means that it corresponds to a different grid than the one given in figure 4 and table A-4. Also, nanohills and surface texturing defined in literature are possibly observed in this report [22, 23]. These will be reffered to as microstructural change

Damage of Si-Si$_y$N$_x$ and Si-SiO$_2$-Si$_y$N$_x$ samples are investigated. Multiple regimes with different damage morphology/mechanism are seen while doing so and shown in figure 3. As a preliminary summary of findings, regions are enumerated;

1. amorphization of Si (yellow color visible with Bright Field Microscopy in figure 3, supported by literature [33])
    - 1.1 possibly Si native oxide melting (orange color visible with Bright Field Microscopy in figure 3, supported by literature [33])
2. edges of delaminted Si$_y$N$_x$ (visible in Dark Field Microscopy figure 4)
    - 2.1 molten Si or microstructural changes underneathSi$_y$N$_x$ (visible in AFM figure 16 and SEM in figure 15)
    - 2.2 region 2.2 = microstructural changes (visible in AFM figure 16 and SEM visible in figure 15)
3. Si ablation edge of delamination of Si$_y$N$_x$ (visible with AFM in figure 16)
    - 3.1 phase change region (visible in AFM figure 16, Bright Field Microscopy and SEM in figure 3
    - 3.2 recrystalization of Si (supported by literature [33], visible in Bright Field Microscopy in figure 3)

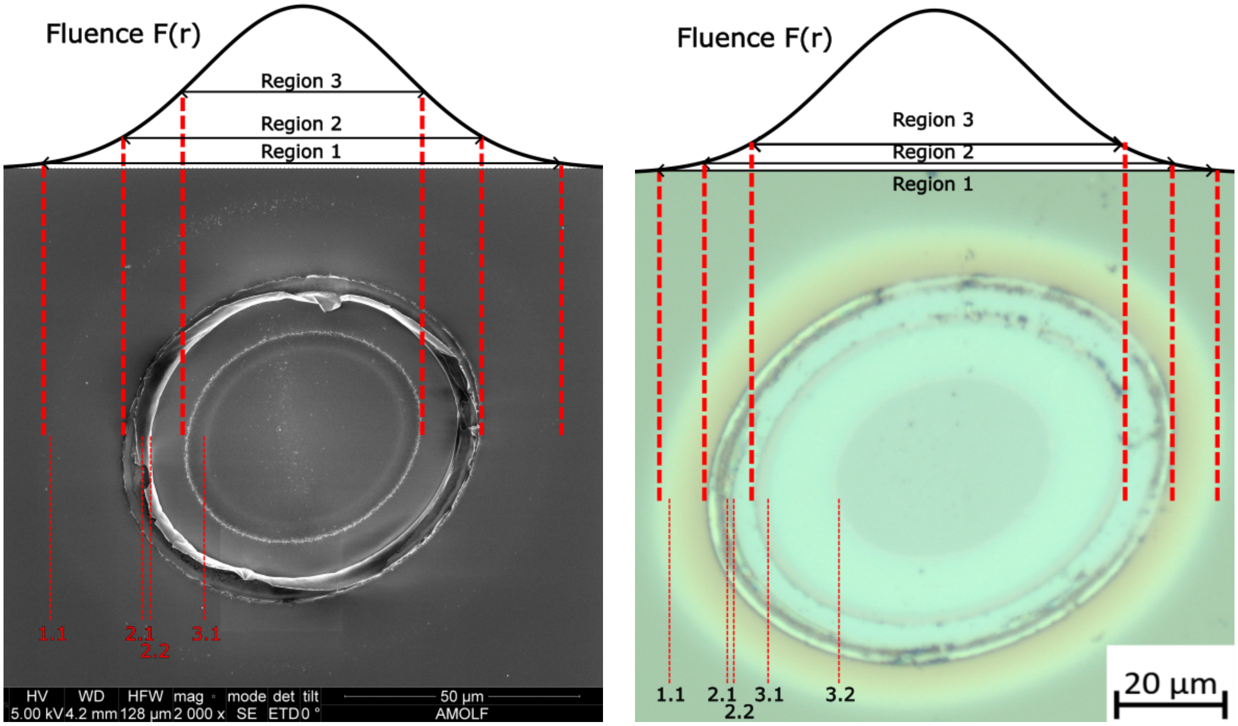

(a) SEM image of spot with fluence F = $0.37\frac{J}{cm^2}$ (b) Bright Field image of spot 13 with fluence F = $1.29\frac{J}{cm^2}$

Figure 3: a) SEM image at fluence of F = $0.37\frac{J}{cm^2}$, with a Gaussian on top indicating the fluence distribution as a function of position. Parameters of SEM are given in the bottom black box. Region 1 edge = yellow ring in Bright Field Microscopy (figure 4), region 2 edge = outer edge visible in Dark Field Microscopy, region 3 edge = ring visible in AFM (figure 16)). Bright square at bottom is likely carbon. b) Same gaussian is placed on top of Bright Field image. The image use 50x zoom and corresponds to spot 13 in figure 4. Colors yellow and orange can be seen between region 1 and region 2.

5.1 Dark Field and Bright Field Microscopy for Si-Si$_y$N$_x$ sample

After performing the damage measurement as described in section 4, the damaged sample is imaged using Dark Field and Bright Field Microscopy, where the cleaned Si-Si$_y$N$_x$ sample and a measurement grid of it can be seen in figure 4 (a complete list of corresponding fluences to each spot is given in table A-4). Cleaning is described in section 4.2 and, unless mentioned, all data precedes from a cleaned sample for Si-Si$_y$N$_x$ (not Si-SiO$_2$-Si$_y$N$_x$). Focusing first on the Dark Field image, small irregularities can be seen inside the ablation rings. Since Dark Field Microscopy enhances scattered light, the origin of those irregularities could be surface modifications or micro particle debris scattering. However, it's more likely to be surface modification, which can be seen by comparing the cleaned Dark Field Microscopy figure 4 of Si-Si$_y$N$_x$ to the uncleaned Dark Field in figure A-22. Micro-particles debris are successfully removed at the sides of the ablation rings, but not at the center, showing micro-particles are not the main source of scattering at the center, leaving surface modification as the likely alternative. As for the ellipses at the top and bottom of the ablation rings at high fluence, these are due to a bad beam profile, but can be ignored as the Gaussian shape is maintained at the center (And high fluences are filtered out during Liu analysis). Bad beam profile is only visible at higher fluences since it's proportion out of the total beam is low.

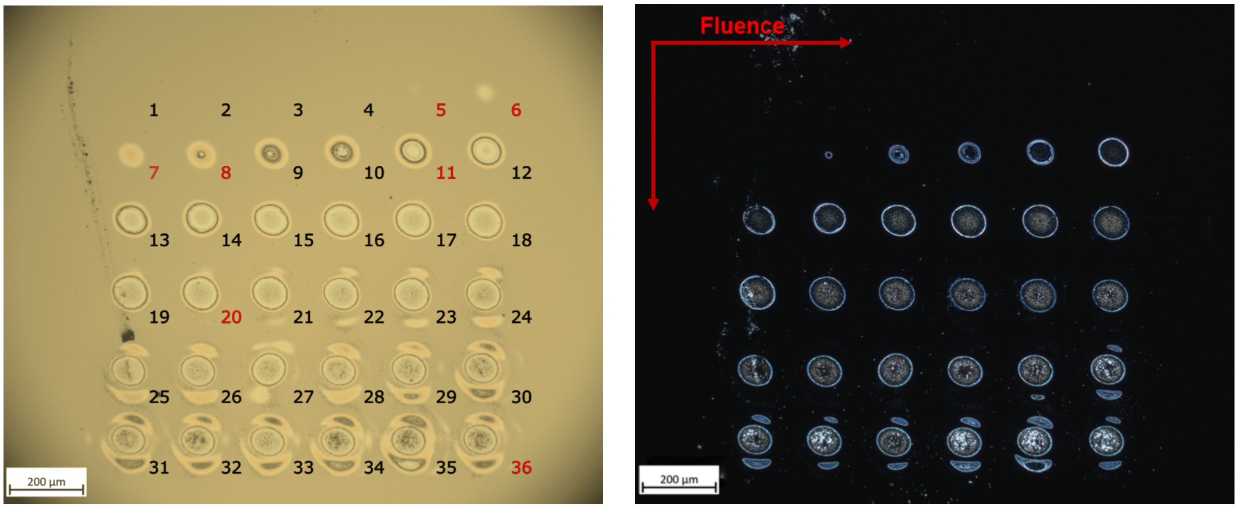

(a) Bright Field

(b) Dark Field

Figure 4: Bright Field (a) and Dark Field (b) Microscopy images of Si-Si_yN_x after cleaning with water and isopropanol in an ultrasound bath. a) sample is illuminated from the top, and reflected light is measured. Mark visible at the left is likely a scratch (did not influence measurements). The numbers to the lower left of the irradiation spots indicate the spot number. If the number is red, it means this spot is studied further b) sample illuminated from top at an angle, then scattered light is measured. a) image is compressed

Another relevant observation for low fluence Dark Field Microscopy are the ablation rings in the second row. It can be seen that an outer ring is always present, but an inner ring forms and expands with increasing fluence (this also applied for the outer ring). This inner ring could indicate delamination of Si_yN_x, which is investigated at spot 8 with AFM in section 5.8.2 and SEM in section 5.8.1.

For low fluence, Dark Field Microscopy only shows damage onwards of spot 8 (row 2, column 2), which corresponds to a fluence of $F_{spot8} = 0.44\frac{J}{cm^2}$. However, Bright Field Microscopy shows signs of damage starting at spot 5 (row 1, column 5) with a fluence of $F_{spot5} = 0.16\frac{J}{cm^2}$. This can be understood by considering the sensitivity of Dark Field Microscopy to surface scattering, indicating a lack of surface modification at the spots only visible in Bright Field Microscopy.

There are many possible explanations for this, which could all be playing a role simultaneously, such as Si crystal/amorphous phase change, Si "bubble" formation due stress in Si, "air bubble" formation due to to stress/molten/plasma/hydrodynamics Si, damage in Si_yN_x, pressure induced material change, partial delamination, micro-damage due to Coulomb Explosion in Si or Si_yN_x, shock waves, etc. "Bubble" formation refers to bulging upwards, where the bulge can be filled with material "Si or Si_yN_x bubble" or be hollow ("air bubble").

5.2 Reflectance Microscopy for Si-Si_yN_x sample

Reflectance Micoscopy is used to obtain reflectance spectra at the center of each irradiated spot. The spectras are averaged over the 8 measured grids. The spectrum of each spot in a grid is given in figure 5 with the respective variances in table A-3. At low fluence (spot 1-4) for Si-Si_yN_x sample, the reflectance spectra matches closely with the simulated reflectance spectra in figure A-26. Also, there seems to be no variation in spectrum for spots 1-4. This matches the absence of color change in Bright Field Microscopy (figure 4) at the same spot. However, at higher fluences (spot 5-7), change in Bright Field images and spectrum appear. This is initially apparent by the peak in the spectrum at 400-500nm at spot 5-7. These measured peaks most likely correspond to crystal/amorphous phase change in Si as shown in literature [34, 35]. However, it can also be argued that an "air bubble" (hollow layer between Si and Si_yN_x) could cause it. In section 5.6 it's shown that this is unlikely via Fresnel transfer matrix multilayer simulations.

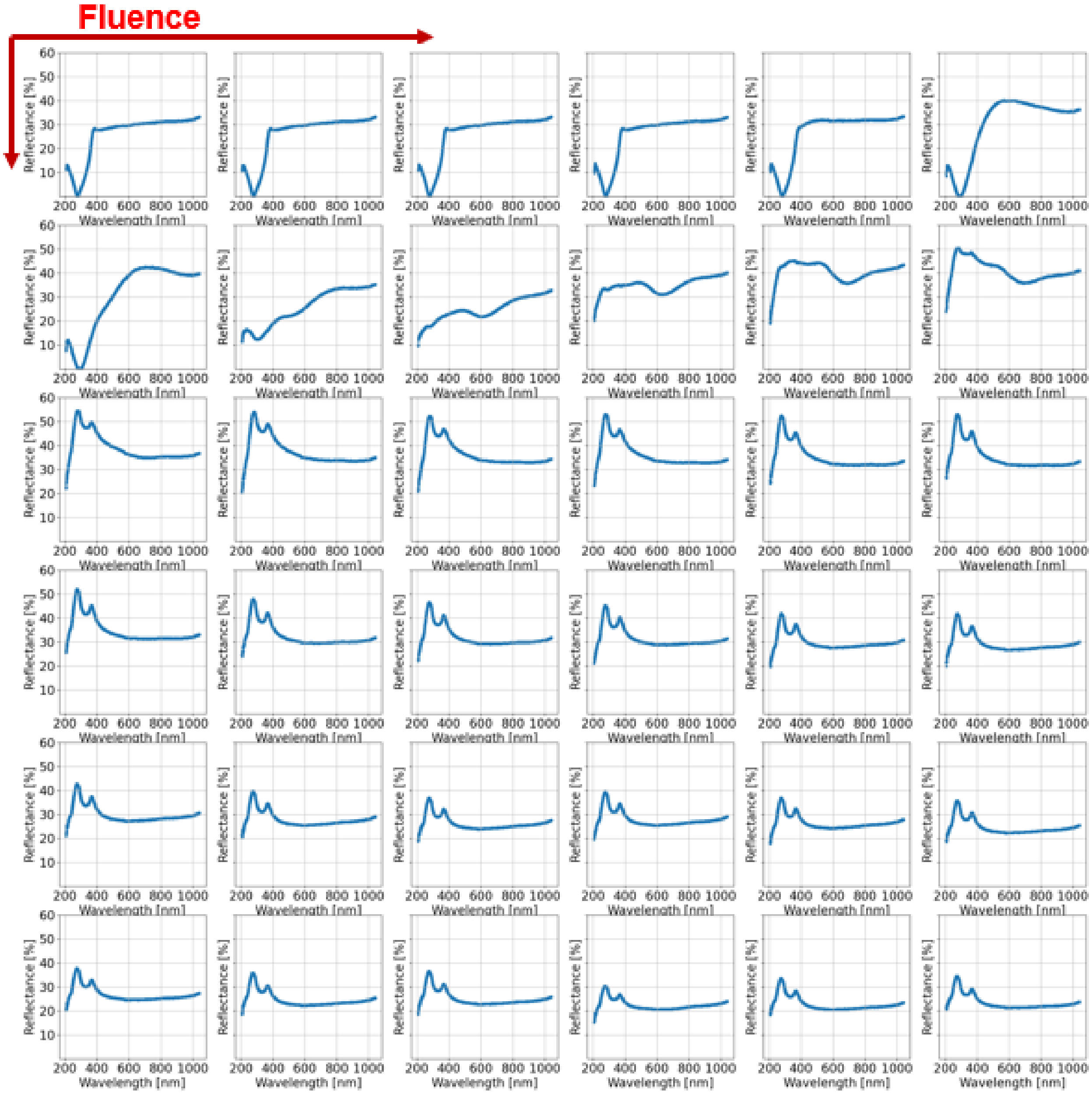

Figure 5: Reflectance spectra of Si-Si$_y$N$_x$ sample for increasing fluence. The figure is made by averaging 8 grids. Each spot corresponds to the one visible in Bright Field Microscopy in figure 4. Variances are given in table A-3

For fluences at spot 8-11, a change in spectrum shape is observed, which corresponds to the ablation fluence where change is visible in dark field Microscopy (figure 4). Furthermore, a dip appears at wavelengths 500-700nm. Interestingly, this dip is similar to the ones obtained for Si reflectance spectra as seen in figure A-25 at similar fluences. The fluences are listed in table A-4 and should be corrected with absorptions in table 5.6 to account for different refletivities.

For spots 13-36, a constant spectral shape is maintained, where the interesting feature is the double peak at 275 and 370 nm, which barely changes with fluence. This double peak matches the one measured in bare silicon in figure A-25, and those found in literature [36]. This serves as indication of Si$_y$N$_x$ delamination/removal. It can also be seen that, after delamination of Si$_y$N$_x$, the reflectivity decreases overall for higher fluences, which can be attributed to increased surface scattering as seen with Dark Field Microscopy (figure 4). This increase in scattering correlates to pits shown with AFM in figure A-40, which increase in size.

5.2.1 Si-Si$_y$N$_x$ reflectance

Besides using the refletcance microscope, photodiodes are also used to obtain the reflectance difference after a pump shot. Figure 6 shows the reflectance given as

$$R_{before} = \frac{\sum_{n=1}^{999} \frac{S_{R,pr,n}}{S_{ref,pr,n}}}{999} \qquad R_{after} = \frac{\sum_{n=1001}^{2000} \frac{S_{R,pr,n}}{S_{ref,pr,n}}}{1000} \tag{11}$$

$$\Delta R = \frac{R_{after} - R_{before}}{R_{after}} \tag{12}$$

where n is the probe shot number (1ms between probe pulses), R(before) is the average reflectance of 999 probe shots before the pump pulse is incident, then the probe pulse coinciding with pump is discarted. R(after) is the average reflectance of 1000 probe shots after the pump pulse has hit the sample. Although more data is needed, it can be seen that a decrease in relfectance occurs for higher fluences, which matches with the trends from the reflectance microscope in figure 5. Also, reflectance seems to start increasing at $0.126\frac{J}{cm^2}$, which corresponds closely to the threhsold obtained via Liu analysis of region 1 with fluence $F_{abl,yellow} = 0.13575\frac{J}{cm^2}$ shown section 5.5.

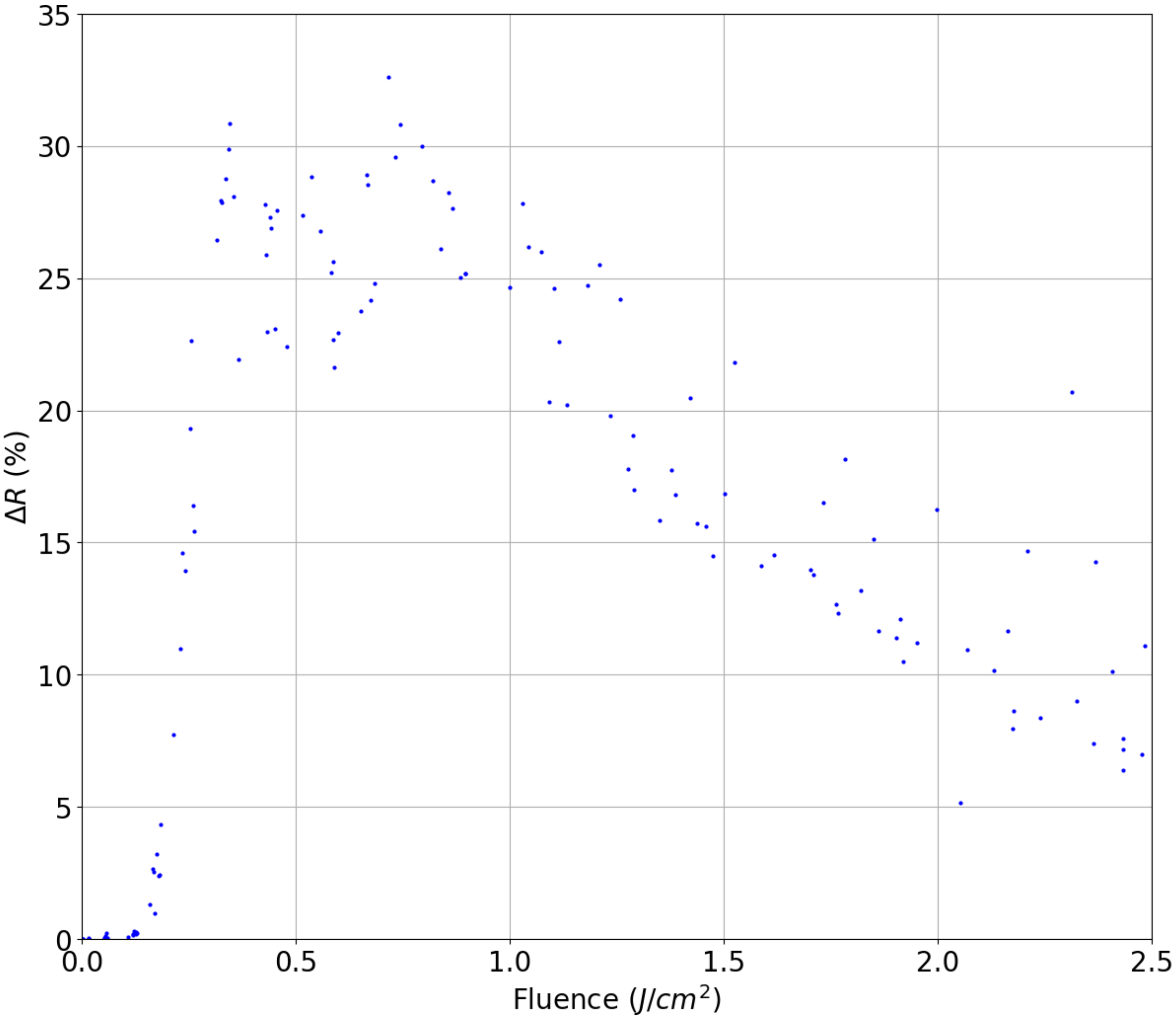

Figure 6: Reflectance as a function of fluence for 8 grids. Data compares the average reflectance of the surface before the pump shot and after the pump shot for 1s each respectively.

5.3 Dark Field and Bright Field Microscopy Si-SiO$_2$-Si$_y$N$_x$ sample

For the Si-SiO$_2$-Si$_y$N$_x$ sample, changes in Bright Field Microscopy appear sooner than changes in Dark Field Microscopy as seen in figure 7, which is similar to the behavior of Si-Si$_y$N$_x$ sample in figure 4. The beam spot size is bigger and the beam shape has no more aberration as explained in section 4. A key difference however is the appearance of an extra ring visible in Dark Field Microscopy, which corresponds to delamination of SiO$_2$.

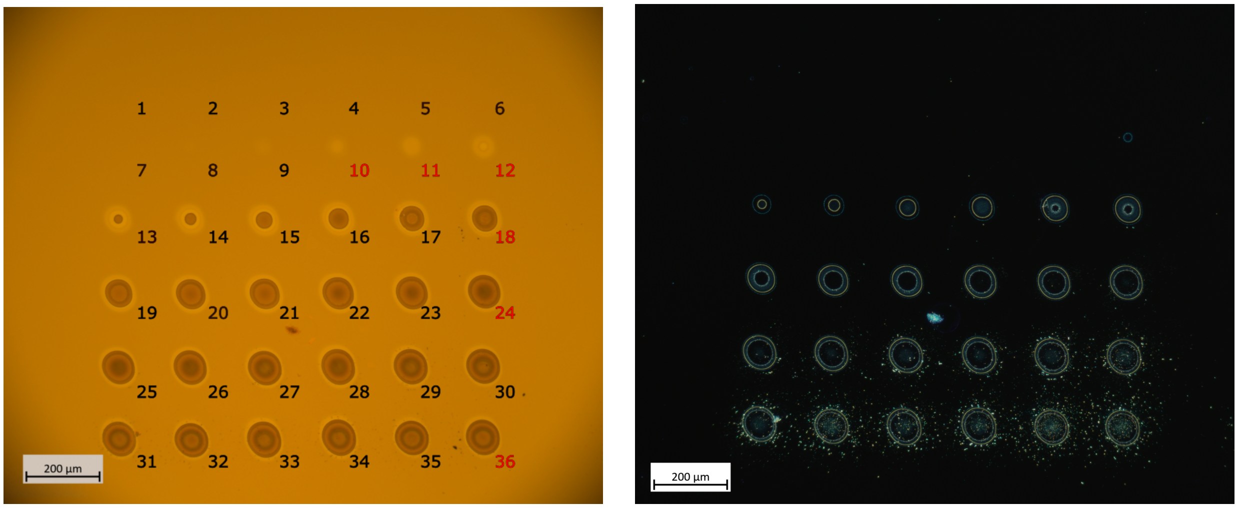

(a) Bright Field

(b) Dark Field

Figure 7: Bright Field (a) and Dark Field (b) images of Si-SiO$_2$-Si$_y$N$_x$ (not cleaned). a) sample is illuminated from the top, and reflected light is measured. Mark visible at the left is likely a scratch. The numbers to the sides of the irradiation spots indicate the spot number. If the number is red, it means this spot is studied further b) sample illuminated from top at an angle, then scattered light is measured. a) image is compressed

5.4 Reflectance Microscopy for Si-SiO$_2$-Si$_y$N$_x$ sample

For the Si-SiO$_2$-Si$_y$N$_x$ sample, the reflectance spectra is taken (figure 8) and averaged over 9 grids (variances given in table A-3). At low fluence (spot 1-9) for Si-SiO$_2$-Si$_y$N$_x$ sample, the reflectance spectra matches closely with the simulated reflectance spectra in figure A-26. There's little variation in spectrum until spot 9, which matches with Bright Field (figure 7).

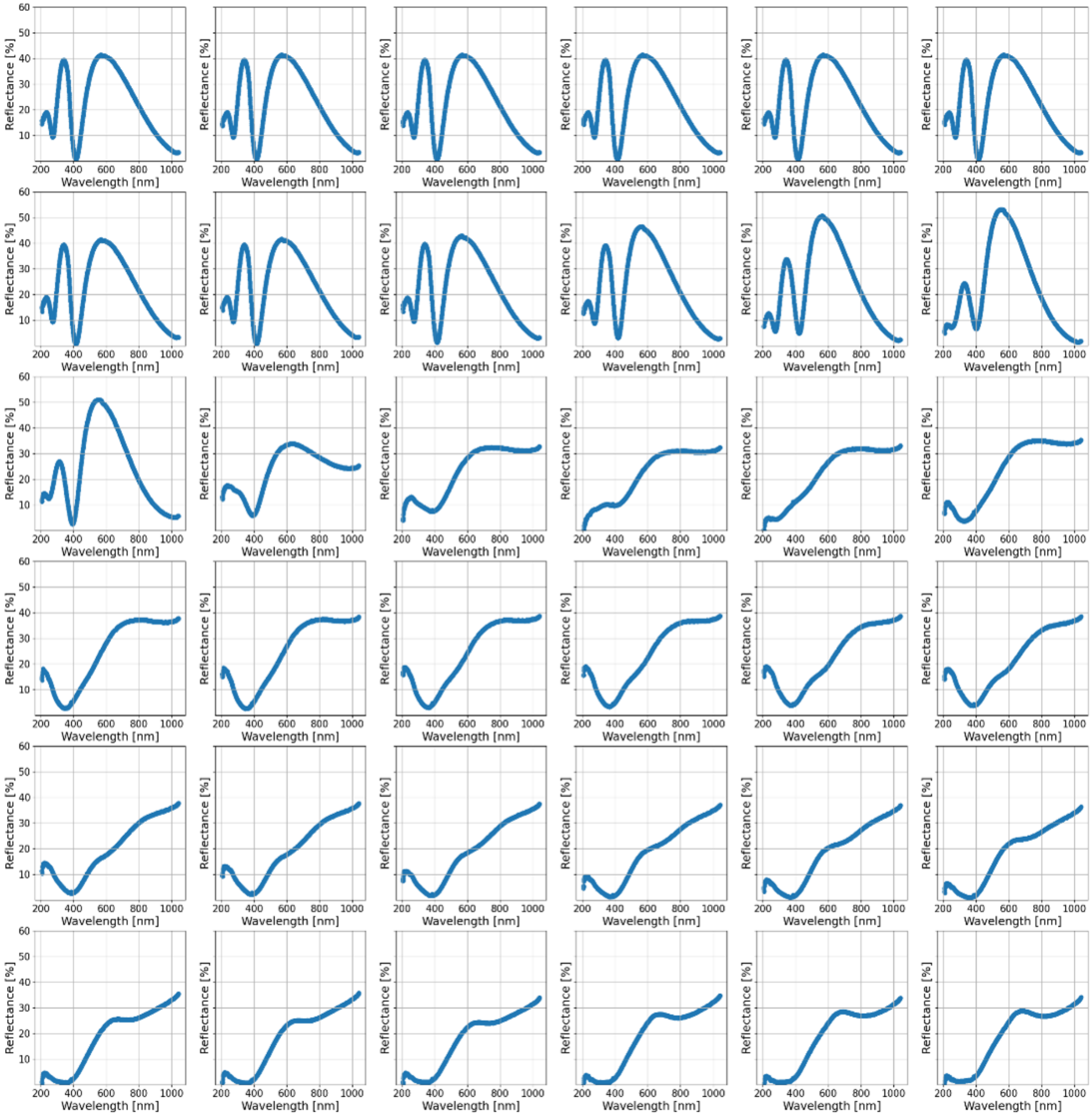

Figure 8: Reflectance spectra of Si-SiO$_2$-Si$_y$N$_x$ sample for increasing fluence. The figure is made by averaging 9 grids. Each spot corresponds to the one visible in Bright Field microscopy in figure 7. Variances are given in table A-3

Also, the peak and dip at 560nm and 395nm seem to be caused mostly be interference, which is verified with the optical path difference in the interference equation

$$(2m+1)\pi = \frac{2\pi}{\lambda} n_i (x_2 - x_1) cos(\theta_i) + \Delta\phi, \tag{13}$$

where m is the mode number, λ incident wavelength (300-1000nm), n_i refractive index of a specific layer, $x_2 - x_1$ is the optical path difference between an immediately reflected beam and a beam propagating through the layers and reflecting on Silicon substrate, θ_i is the angle of incidence (normal in this case), $\Delta\phi$ is the phase difference due to reflection per layer. Equation 13 does not take into account complex refractive indices, which in this doesn't affect the calculation in a major way, since the complex refractive indices is nearly null as seen with ellipsometry in figure A-24. Also, this is only used to obtain an explorative idea of the reflectance spectrum.

No conclusions can be made on the reflectance spectrum for higher fluences. However, possible causes could be absence of interference, new interference due to partial delamination, material change in Si$_y$N$_x$ (due to high absorption as seen with simulations in table 5.6). Counterintuitively, the Si peaks observed for Si-Si$_y$N$_x$ sample in figure 5 are no longer present.

5.5 Liu analysis

The theory for Liu analysis is described in section 3. It's implemented by obtaining the contour area of each ablation spot in Dark Field Microscopy for every grid. This is done via Canny edge detection algorithm, where the outer ring is identified. Aftwerwards high fluences are filtered out. This is necessary since for higher fluences, area to fluence dependence stops being linear due to damage saturation and bad beam profile. Lastly, certain spots are removed manually whenever the Canny algorithm clearly fails. The results are displayed in figure 9, showing the obtained ablation fluences of $F_{abl} = 0.262\frac{J}{cm^2}$ for Si-Si$_y$N$_x$ and $F_{abl} = 0.1433\frac{J}{cm^2}$ for Si-SiO$_2$-Si$_y$N$_x$ sample.

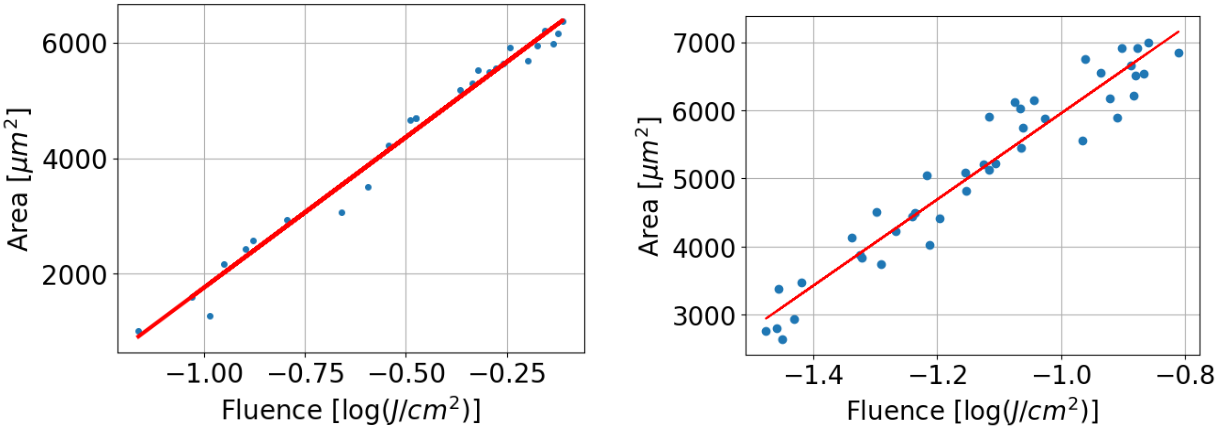

(a) Si-Si$_y$N$_x$$F_{abl} = 0.262\frac{J}{cm^2}$

(b) [Si-SiO$_2$-Si$_y$N$_x$ $F_{abl} = 0.1433\frac{J}{cm^2}$

Figure 9: Plot of ablation area (edges in Dark Field Microscopy in figure 4), against fluence in logarithmic scale for Si-Si$_y$N$_x$ and Si-SiO$_2$-Si$_y$N$_x$ sample. The red line is the linear fit of Liu analysis, and gives the ablation fluence.

Until now only the fluence in Dark Field Microscopy at the edge is considered, however, the fluence at the edges of Bright Field can also give interesting trends, such as the exact fluence at which a material changes (distinguishible by yellow, orange and dark color in bright field). To obtain the fluence at the edge of an ablation spot, equation 3 is used, but converted to calculate fluence at an edge in Bright Field as $F_{local} = Fexp(-\frac{R_x^2 4ln(2)}{\sigma_x^2})$. Also diameters from the yellow and orange ring are used from bright field microscopy in figure 4. An important note is that this calculation is done in 1D, manually and for 1 grid instead of 2D, via an algorithm and for all grids, like previously calculated Liu ablation threhsold in figure 9 due to lack of time. The fluence threhsolds are again calculated with Liu analysis and give $F_{abl,dark} = 0.2181\frac{J}{cm^2}$, $F_{abl,orange} = 0.1619\frac{J}{cm^2}$, $F_{abl,yellow} = 0.13575\frac{J}{cm^2}$. The data used for fitting is available in figure A-23 for Si-Si$_y$N$_x$ sample. Despite the shortcomings of the implementation due to lack of time, these results can still be used since the ablation fluence calculated with this method of $F_{abl,dark} = 0.2181\frac{J}{cm^2}$ is close the previously calculated one of $F_{abl} = 0.262\frac{J}{cm^2}$.

5.6 Multilayer simulations

Fresnel transfer matrix simulations are performed as described in literature [37]. These simulations are done under the assumptions of normal incidence, 50nm FWHM with central wavelentgh 400nm Continuous Wave (CW), no layer diffusion, no surface roughness, material modification, no non-linear effects, no laser speckle effects. The refractive indices and thicknesses were obtained with ellipsometry 4.3.5. Indeed simulations match results obtained with reflectance micrscopy in section 5.2 as seen in figure A-26, indicating that the simulations closely matches reality.

Firstly, absorption per layers is calculated with the absorption profile in figure A-27 and indicated in the table 5.6. It can be seen that for the Si-Si$_y$N$_x$ sample, absorption in Si dominates, suggesting it plays a dominant role. For the Si-SiO$_2$-Si$_y$N$_x$ sample, Si$_y$N$_x$ absorption is considerably higher.

Layer	**Si-Si$_y$N$_x$ Absorption (%)**	**Si-SiO$_2$-Si$_y$N$_x$ Absorption (%)**
Si	70.0497 (substrate)	57.3993 (substrate)
Si native oxide	0.3367 (2nm)	0.8790 (2nm)
SiO$_2$	-	10.4578 (18.6nm)
Si$_y$N$_x$	1.4862 (21.5nm)	31.2637 (121.3nm)

Table 2: Table indicating absorption % (not normalized for reflectance) in each layer of Si-Si$_y$N$_x$ and Si-SiO$_2$-Si$_y$N$_x$ samples, as well as the corresponding thickness besides it. It uses normal incident light at central wavelength of 400nm and 50nm FWHM. Si-Si$_y$N$_x$ sample has no SiO$_2$ indicated as a "-". Table is not normalized, meaning all light that is not absorbed is reflected instead (transmission = 0%).

Additionally, simulations of an "air bubble" (hollow material layer below Si$_y$N$_x$) are performed. Figure 10 shows the Mean Square Error (MSE) for different thicknesses of an "air bubble". This calculation is done in the wavelength range of 370-520nm because measured reflectance spectrum (figure 5) at spots 5-7 has different shapes outside those wavelengths as seen in the figure A-28 (measured plot has a peak at spot 5-6, simulated doesn't). An explanation for this could be that instead of an "air bubble" being responsible, it could be due to Si crystal/amorphous phase change. Literature finds the same peak at a similar wavelength [34,35]. Also, MSE calculation, spot 7 is used as this is the spot before ablation, making it the most likely candidate for "air bubble". However, the most likely thicknes of the air bubble would be 18nm. This thickness is not seen with AFM (spot 6 in figure A-36), giving a strong indication that an "air bubble" is not present.

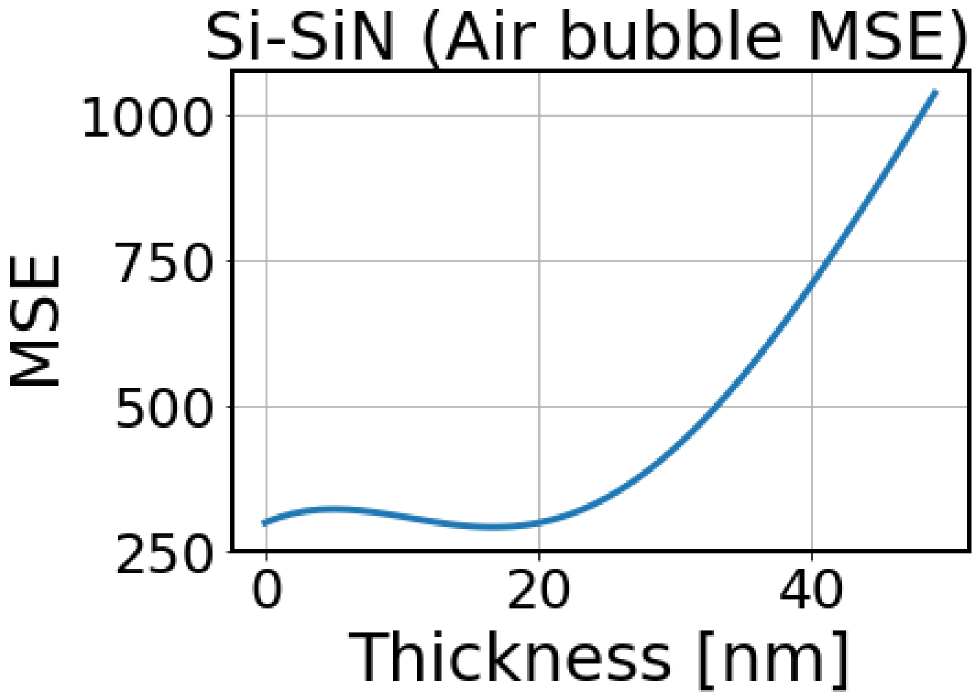

Figure 10: Multilayer simulation Si-Si$_y$N$_x$ sample adding an "air bubble" (hollow in layer in between Si$_y$N$_x$ and Si$_{native}$). Mean Square Error (MSE) with units nm^2 is shown with respect to measured reflectance spectra 5 at spot 7 for different simulated "air bubble" thicknesses. The wavelengths used are 370-520nm since spectral shape differs beyond those wavelengths as shown in figure A-28

5.7 Morphology study Si-Si$_y$N$_x$ spot 6 and 7

5.7.1 Scanning Electron Microscopy

The Si-Si$_y$N$_x$ sample is placed after the damage measurement under the Scanning Electron Microscope (SEM) to obtain small features. A pristine site is shown in figure A-29. Figure A-31 shows the rings visible in Bright Field (figure 4) despite those not being visible in Dark Field Microscopy. Taking into account that SEM images the charging of a material at the surface (among others), this could indicate that material change visible due to a change in conductivity. As discussed in 5.6, Si is the most likely material to have undergone a crystal/amorphous phase change due to Si$_y$N$_x$ being mostly a non-conducting insulator, and damage being unlikely in Si$_y$N$_x$ given its high transparency (table 5.6).

5.7.2 Atomic Force Microscopy

Atomic Force Microscopy (AFM) is used to characterize the damage depth, material phase, microstructural changes and damage regimes among others. Starting at spot 1-6 in figure 4, AFM shows no change in height or phase, until spot 7 (figure A-36). At spot 7, microstructural changes start appearing as seen in figure 11. It's possible these are impurities instead of mocrostructural since SEM on pristine sites show similar spots (figure A-29). However, the density of these structures is higher at the irradiated site than pristine and doesn't appear for lower fluences as seen in figure A-36 and with SEM in figure 12, increasing the likelihood that microstructural changes are caused by the laser. Another interesting oberservation is that the appearance of microstructural changes can be related to the change in color in Bright Field (figure 4) from yellow to orange. This has not be investigated, but possible causes could be Si oxide melting according to literature [33].

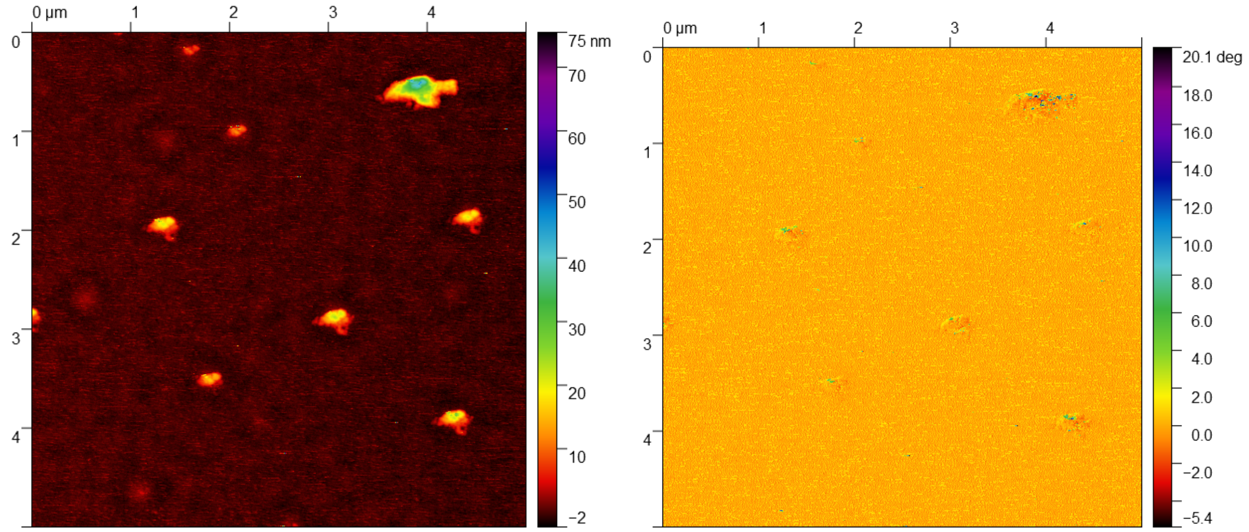

(a) Height (b) Phase

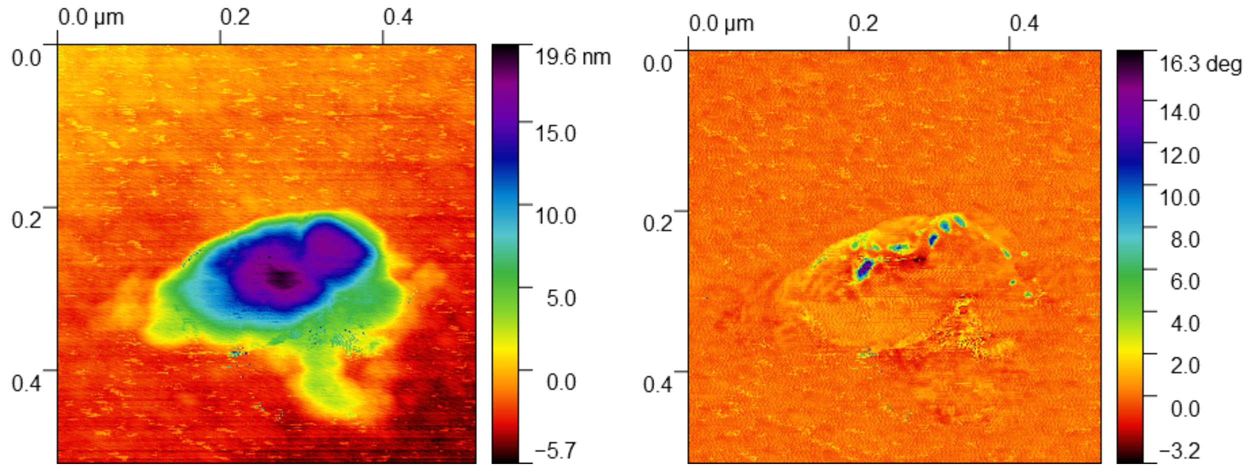

(c) Height (d) Phase

Figure 11: AFM of Si-Si$_y$N$_x$ sample at spot 7 (center), showing a) height and b) AFM phase profile, as well as an AFM scan of a single nanohill showing c) height and d) phase.

Figure 11 also shows single microstructural changes in c) and d). An important observation is the lack of AFM phase change in d) (except at the top, which can be an artifact of AFM due to rapid height change, or slight rupturing/diffusion due to Si). This could mean Si$_y$N$_x$ has not yet been delaminated/ruptured, making it likely a precursor to ablation.

5.8 Morphology study Si-Si$_y$N$_x$ spot 8

5.8.1 Scanning Electron Microscopy

At the next irradiation spot 8, ablation starts appearing (visible in Dark Field Microscopy). Delamination is visible with SEM in figure 12 (as well as the bright edges in figure A-33). It's also possible to observe cracking before delamination as seen in figure A-30, where the fluence is $F = 0.25\frac{J}{cm^2}$, which is close to that obtained via Liu analysis of $0.23\frac{J}{cm^2}$ as shown in figure 9. This suggests that cracking precedes delamination. Besides the reappearing bright rings seen in figure A-33, delamination appears to start at the center of the ablation spot. This delamination then progresses in the outer direction as seen in with the Dark Field Microscopy figure 4 and SEM in figure A-32.

At the center of the delamination ring and at the edges, small circular "nanohills" (or microstructural changes) are observed in figure 12 and figure A-33. The diameter of those at the center and outer edge (outside of delamination ring) are between 187.5nm and 250nm. These nanohills could correspond to those observed with the AFM 11 and those found in literature (nanohillocks [24] and surface texturing [23]). Interestingly, a high concentration of nanohills is present at the inner edges of delamination and underneath the Si_yN_x layer as seen in figure 12 b). This could suggest that the formation of nanohills is related to increasing delamination of Si_yN_x with increasing fluence. To investigate the cause, AFM is used.

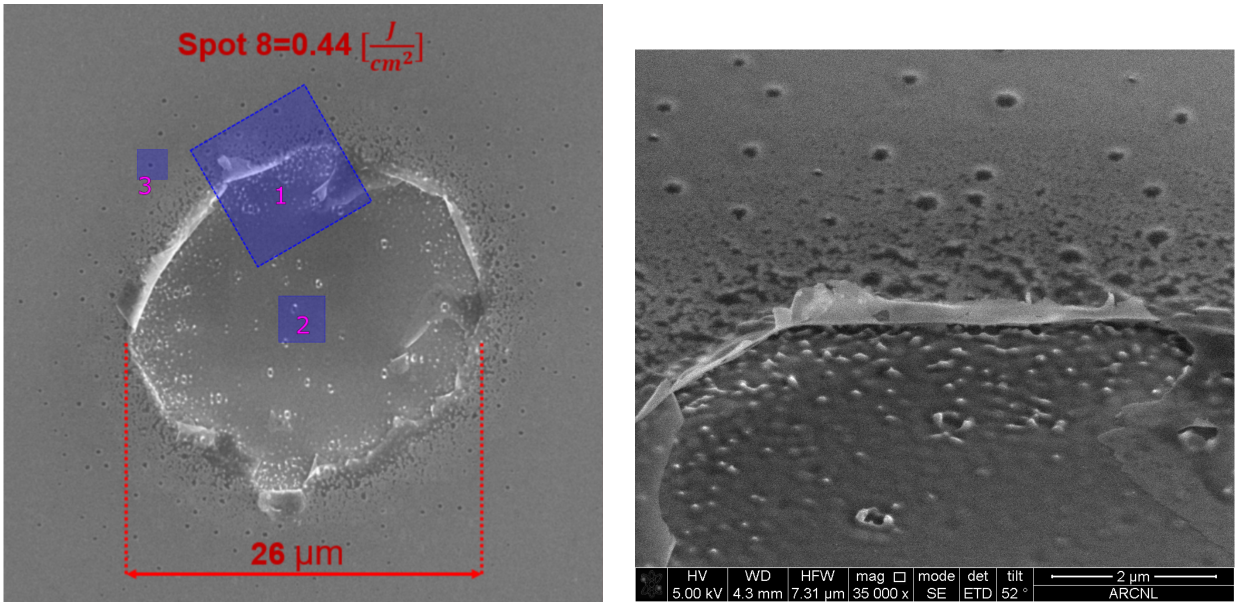

(a) Spot 8 = $0.44\frac{J}{cm^2}$

(b) Spot 8 titled 52°.

Figure 12: SEM image of Si-Si_yN_x of spot 8. a) is zoomed in such that the bright rings are no longer visible. Blue squares (numbered) indicate where SEM and AFM scans are b) is done. b) sample tilted 52 ° at blue square 1 in a).

5.8.2 Atomic Force Microscopy

Furthermore, this is supported by observing the same microstructural changes at ablated spot 8 (center and edge), but with closer spacing and larger dimensions as shown in figure 13. Moreover, circular "pits" with dark centers can be seen with diameter $D = 0.45 \pm 0.05\mu m$ (obtained by averaging by visual inspection). These could show material removal or displacement. Possible mechanisms for this could be phase explosion, coulomb explosion or molten Si redistribution due to stress. However, Coulomb Explosion is somewhat contested in literature, some papers claim Coulomb Explosion is present and dominates damage [22, 24, 38], whereas other papers claim ultra fast melting and phase explosion plays a role [26, 39]. For that reason, no strong claim can be made, but given the similarities in experimental parameters and surface morphology with papers that observe Coulomb Explosion, this process should not be discarted [22]. Besides microstructural changes, it's also possible that nanovolcanoes are seen as shown in figure A-37 and literature with different materials [40].

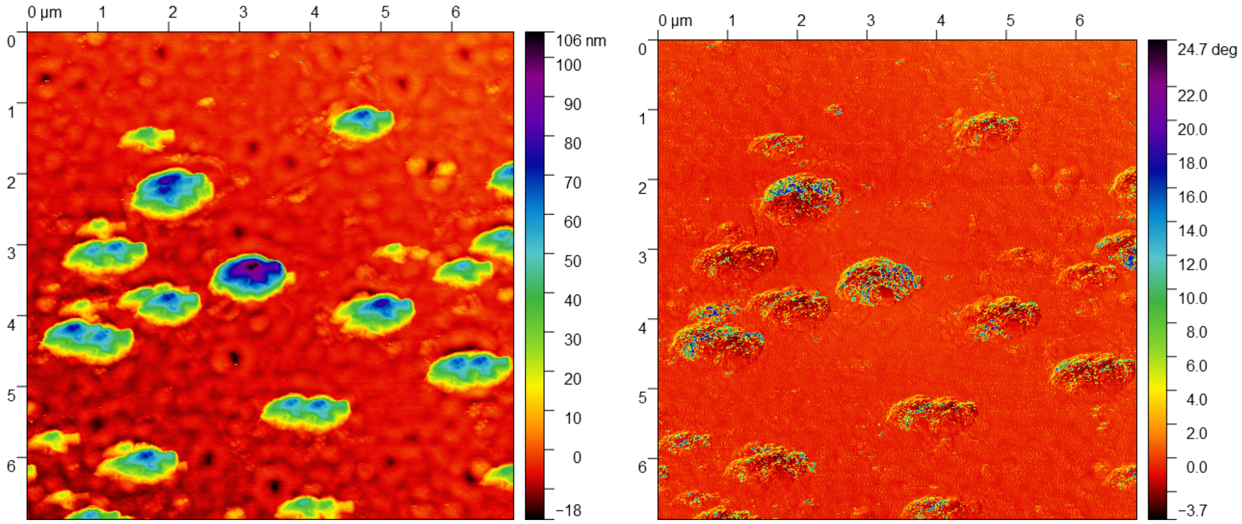

(a) Height

(b) Phase

Figure 13: AFM of Si-Si$_y$N$_x$ sample at spot 8 (blue square 2 in figure 12), showing microstructural changes with a) height and b) AFM phase profile.

To further understand the ablation process, another AFM scan at spot 8 is taken of a nanohill in figure 14, but at the edge of the delaminated part. A sharp peak can be seen together with phase irregularities around the peak, but constant at the top. A possible explanation for this could be ripping of Si through the Si$_y$N$_x$ layer, which would explain the constant phase at the peak and sudden height change at the peak (This still needs to be verified however). Lastly, the height profile is obtained for spot 8 in figure A-39, indicating complete delamination of Si$_y$N$_x$ takes place.

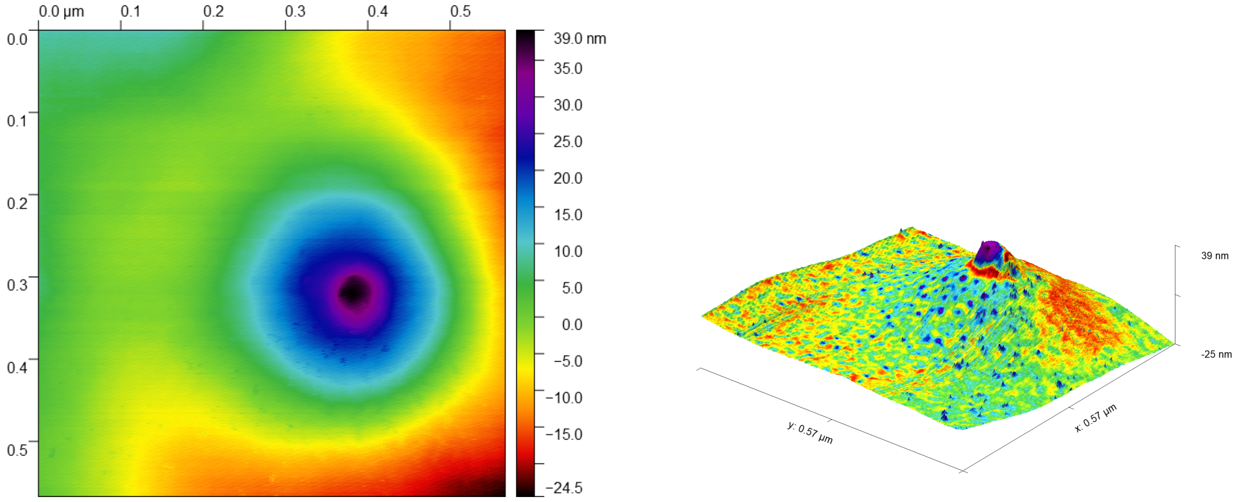

(a) Height

(b) Phase

Figure 14: AFM of Si-Si$_y$N$_x$ sample at spot 8 (position blue box 3 in figure 12). It corresponds to region 1.1-2. showing nanohill with a) height and b) 3D image of the height profile with the colors indicating the phase signal. Plot with only phase is given in figure A-38.

5.9 Morphology study Si-Si$_y$N$_x$ spot 20

5.9.1 Scanning Electron Microscopy

Another spot investigated with SEM and AFM is spot 20 in figure 15. In region 2-2.1, at the bottom, remains of Si$_y$N$_x$ delamination can be seen. The shape of the remains are a hill (fully dark part to the right) and ripple (dark-grey-dark part to the left). No explanation is found as of the date of this report for this. From the ripple/hill to the end of region 2.1, a region with varying dark and grey colors can be seen. This pattern could arise due to microstructural changes such as microstructural changes merging underneath Si$_y$N$_x$ layer. Another possibility is molten Si according to literature [27,33,41]. Between region 2.1 and 2.2, microstructural changes are visible. Between region 2.2 and 3, there's a flat region where Si$_y$N$_x$ has been delaminated, and possibly Si as discussed in spot 8 in section 5.8.2. This is the last region where Si$_y$N$_x$ is attached as seen in figure A-34. Directly at region 3, there's a rapid increase in height as shown with AFM in figure 16

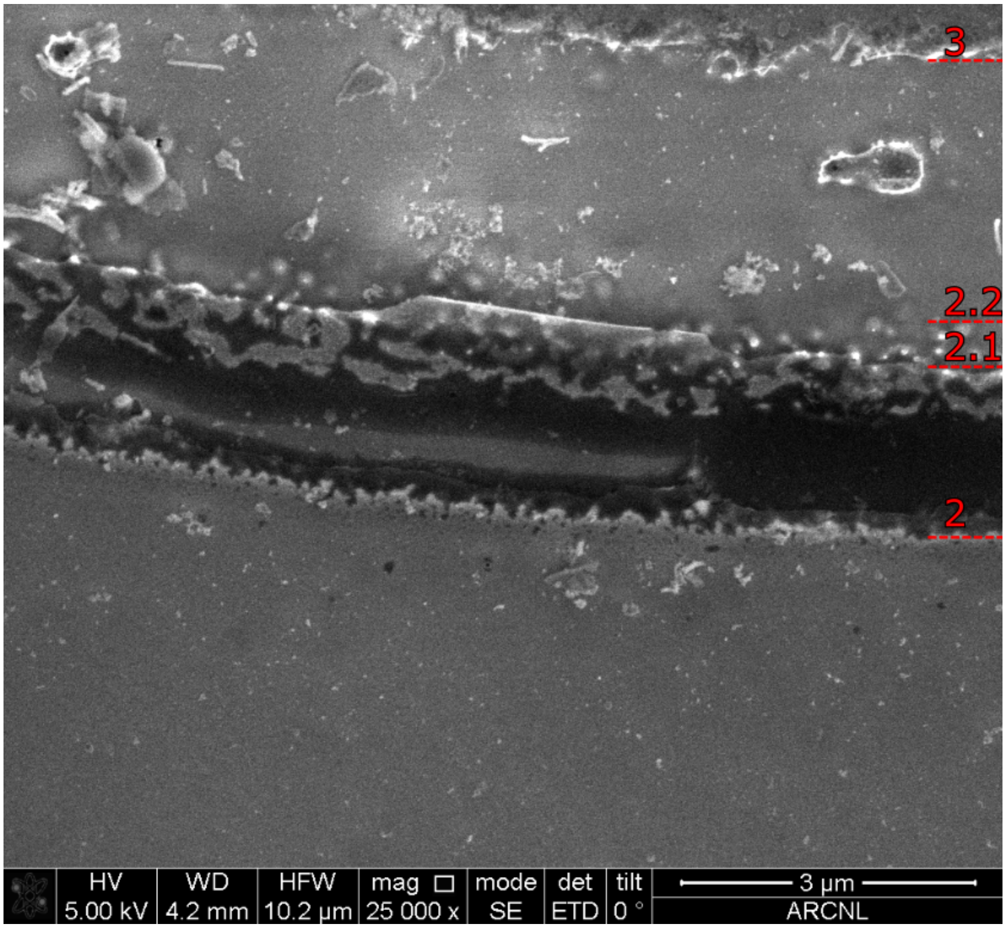

Figure 15: SEM image of Si-Si$_y$N$_x$ of spot 20 F = $2.73\frac{J}{cm^2}$ at the bottom. The regions defined in figure 3 are specified to the right in red.

5.9.2 Atomic Force Microscopy

Figure 16 shows an AFM scan of spot 20 at the bottom edge. For higher fluences, possibly different mechanisms play a role during ablation. First of all, at the top region (center - region 3.1), the same pits are observed but with larger diameter $D = 0.8 \pm 0.2\mu m$. Increase of pit diameter with higher fluence seems to be a consistent trend as shown with the highest fluence AFM image in figure A-40.

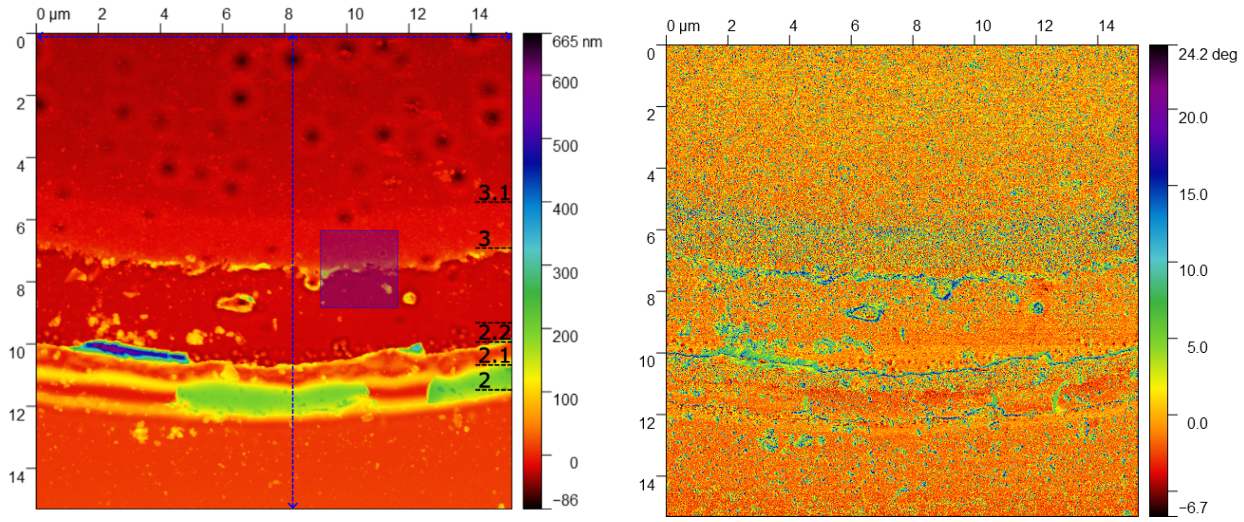

(a) Height

(b) Phase

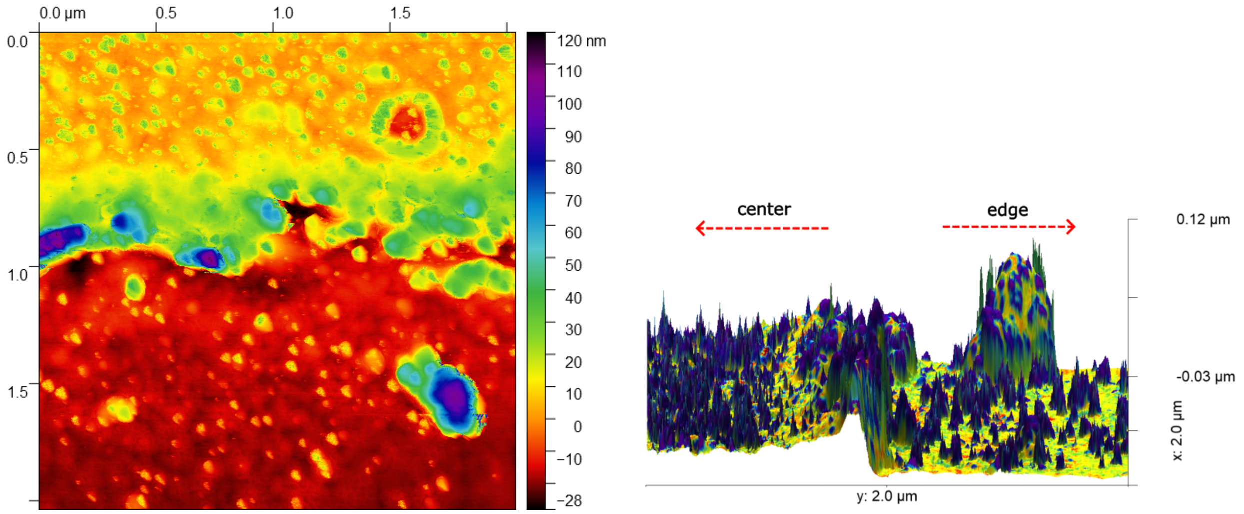

(c) Height

(d) Phase

Figure 16: AFM of Si-Si$_y$N$_x$ sample at spot 20 (bottom ring), showing a) height and b) AFM phase. a) the regions defined in figure 3 are specified to the right of the image. The blue square shows where the AFM scan for c) and d) are done. The blue striped arrows indicate where the height profile is taken in figure 17. c) and d) are AFM scans of same spot, but focused on the blue square in a). c) Height, d) 3D image of the height profile with the colors indicating the phase signal. The two red arrows indicate orientation (left pointing faces center, right pointing faces edge). Plot with only phase shown in figure A-41. Left side is facing center, right is facing region 2.2.

In figure 16, between region 3.1-3, a slight height and phase difference can be seen. To investigate this further, another AFM scan is done at the edge of region 3.1 as shown in figure c) and d) of figure 16. Although not investigated, 2 suggested mechanisms could be the flaps from Si$_y$N$_x$ elevating the edge during delamination. This is supported figure A-34 showing that region 3 is the last contact part before full delamination. Another explanation could be hydrodynamics as supported by literature [42]. Furthermore, between region 3-2.2, there is a regime with constant nearly height and phase as shown in figure 16 and supported by another AFM scan of spot 11 in the same regime in figure A-42.

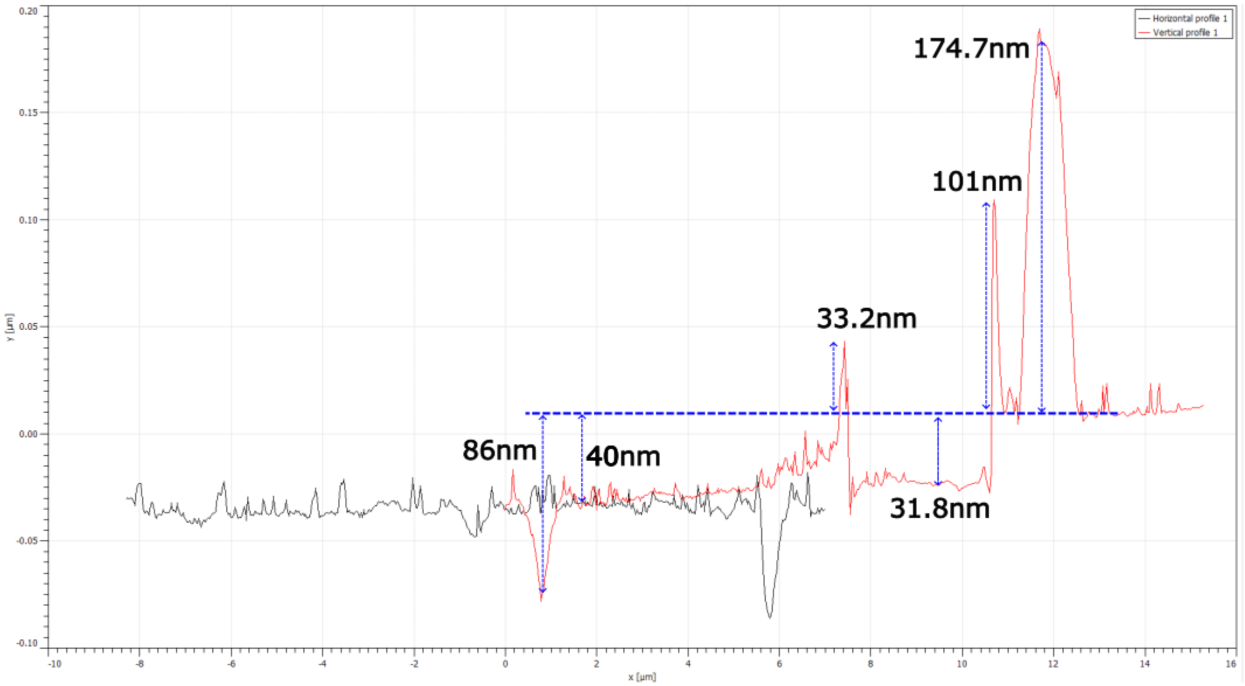

Figure 17: Height profile of Si-Si_yN_x sample (21.3nm Si_yN_x deposited) obtained at the blue stripes in figure 16 a), showing horizontal and vertical height profile across the delaminated site. Heights are indicated with respect to the non-delaminted part (region 2-1.1) with blue stripe.

Figure 17 shows the height profile of spot 20. Since only 21.5nm of Si_yN_x is deposited, a height difference greater than this indicates Si removal. This is the opposite of spot 8, where mainly Si_yN_x is removed as shown in figure A-39. Also, the increasing height of region 3 can be seen and the depth of the pits (which may be deeper since AFM is limited by tip size). The ripples can also be seen, with the outer one being the tallest. It's known that there must be remains of Si_yN_x delamination here, as supported by SEM images in figure A-34. Therefore, the outer most edge is Si_yN_x delamination remnants.

5.10 Morphology study Si-SiO_2-Si_yN_x spot 10 and 11

5.10.1 Scanning Electron Microscopy

The Si-SiO_2-Si_yN_x sample is imaged under the SEM. For spots 10 and 11, no change is visible under Dark Field Microscopy (figure 7). However, surface modication is visible with Bright Field Microscopy for spot 10,11, and SEM for spot 11 as shown in figure A-35.

5.10.2 Profilometer

mechanical Profilometry is used to obtain an estimate of the surface morphology. Changes are clearly visible as shown in figure 18, where spot 11 shows surface modification with a 20nm high bulge, whereas no change is appreciable for spot 10. The bulge of spot 11 doesn't appear centered due to profilometer imprecision, but is verified to be the center more scans (not included).

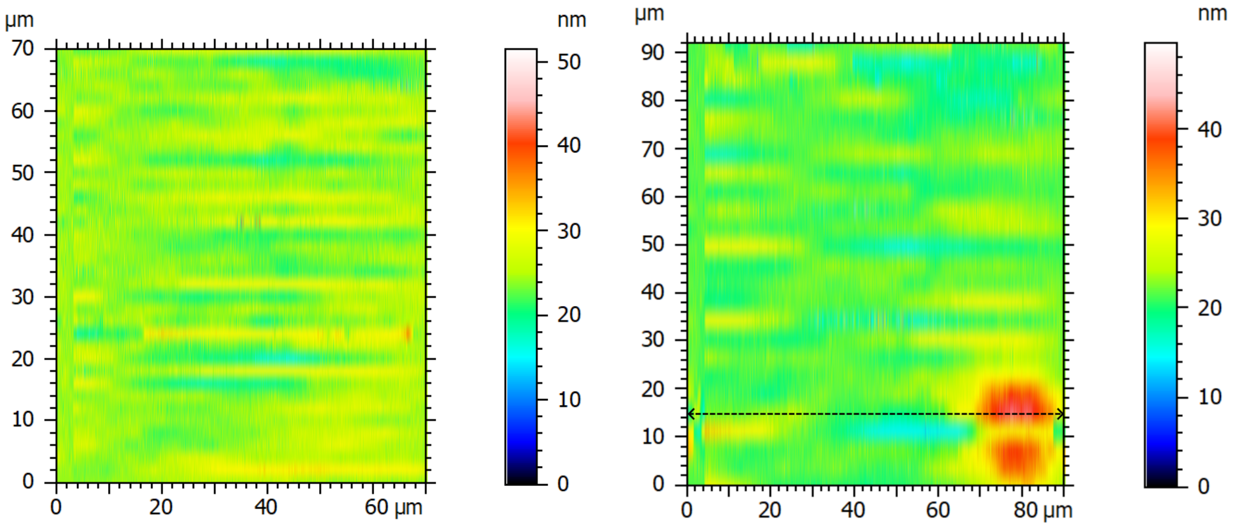

(a) Spot 10 height scan

(b) Spot 11 height scan

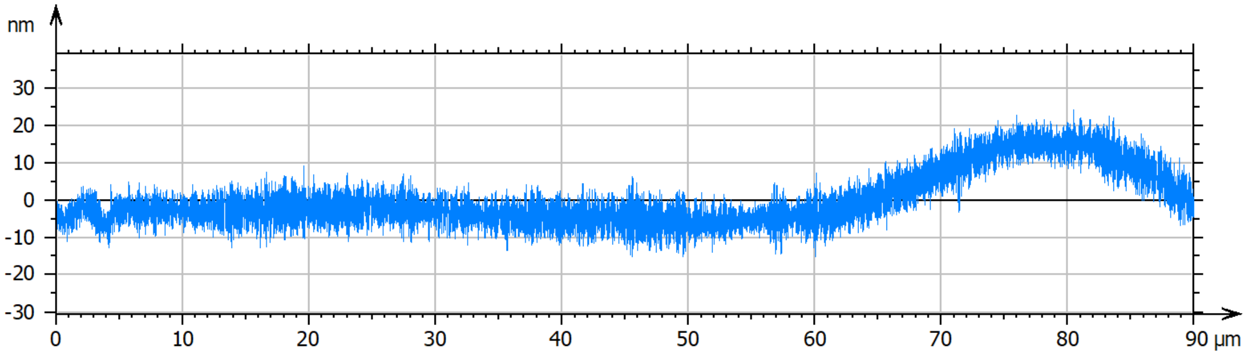

(c) Spot 12 height profile

Figure 18: Height scans of Si-SiO$_2$-Si$_y$N$_x$ sample obtained with Profilometer at spot a) 10, b) 11. c) height profile of spot 11 extracted from the cross section indicated by the black stripes in b). Spot 11 clearly shows a 20nm tall bulge outwards of the surface.

5.11 Morphology study Si-SiO$_2$-Si$_y$N$_x$ spot 12

5.11.1 Profilometer

A donut structure is obtained with a Profilometer for spot 12 as shown in figure 19. This shape has not been observed for the Si-Si$_y$N$_x$ sample. Although the cause has not been verified in this report, a possibility according to literature is hydrodynamics due to molten Si creeping towards the edges and solidifying [42]. This would create edges with higher altitude at the edges than the center.

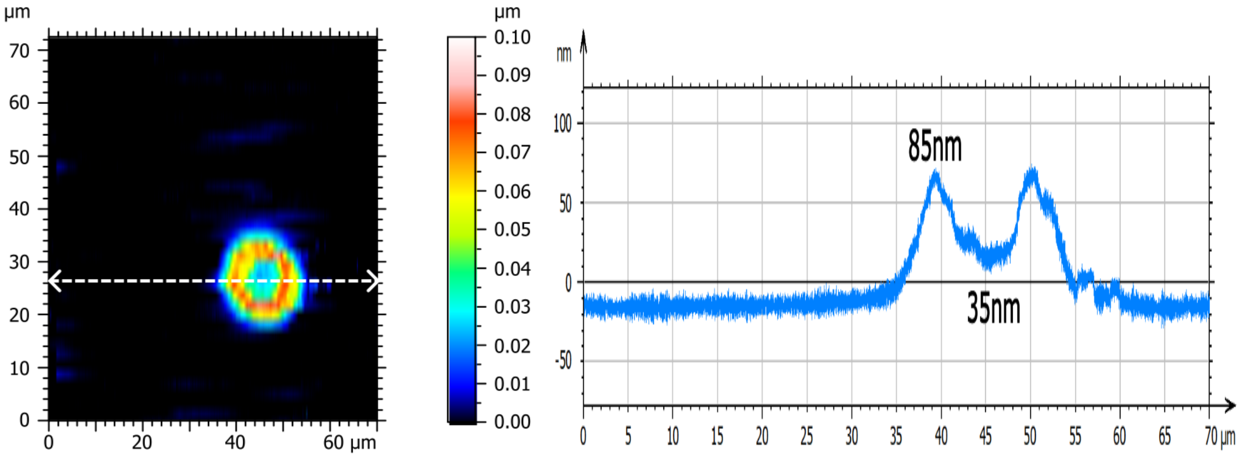

(a) Spot 12 height scan

(b) Spot 12 height profile

Figure 19: a) Height scans of Si-SiO$_2$-Si$_y$N$_x$ sample is obtained with a Profilometer at spot 12. b) height profile at the cross section indicated with white stripes in a). The peaks have approximately a height of 85nm and the center 35nm with respect to the non-ablated parts.

5.11.2 Scanning Electron Microscopy

SEM of spot 12 (figure 20) shows web-like modification in a donut shape. This differs from the bulge at spot 11 (figure 18).

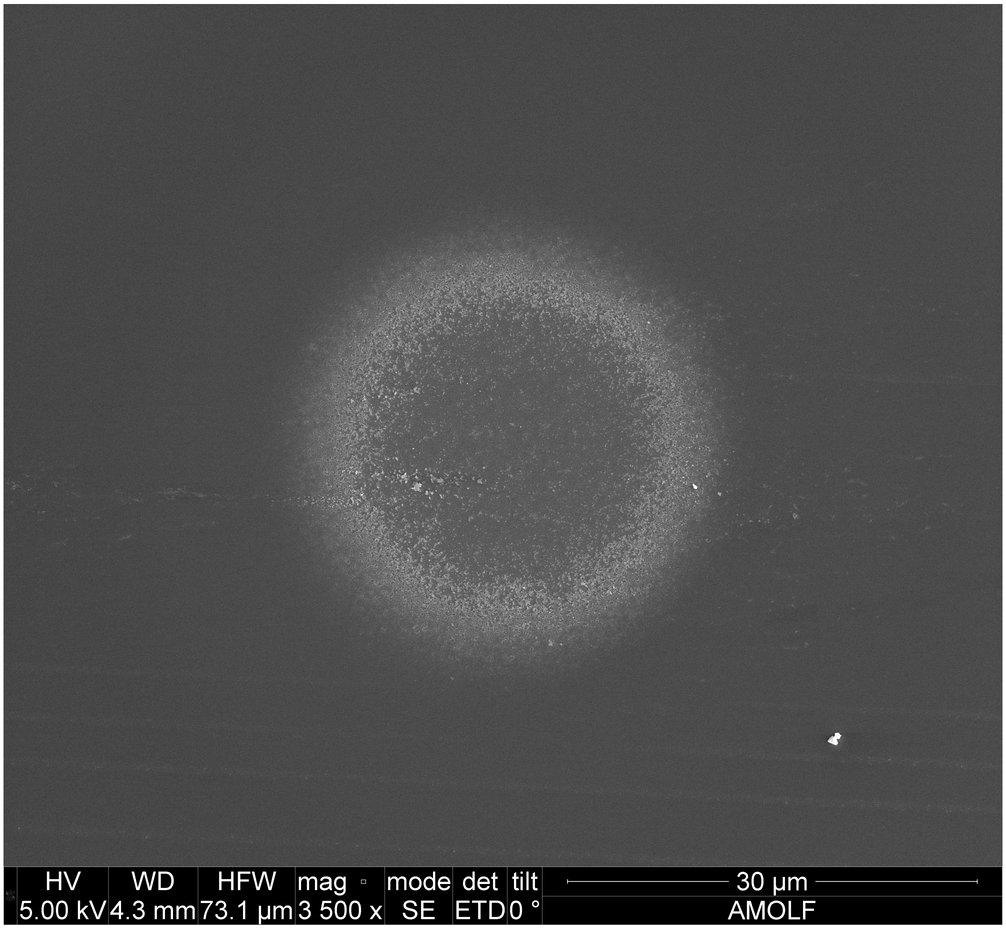

Figure 20: SEM image of Si-SiO$_2$-Si$_y$N$_x$ sample at spot 12. Web-like changes are visible with a donut shape. The horizontal stripes are probably due to Si cutting imperfection and not Light Induced Periodic Surface Structuring (LIPSS) as explained in figure A-43

5.12 Morphology study Si-SiO$_2$-Si$_y$N$_x$ spot 18

5.12.1 Profilometer

Lastly, spot 18 is above the ablation threshold and shows interesting delamination behavior as seen in figure 21. Two cascading craters can be seen (outer crater with peaks 50nm tall, and inner crater with -10nm peaks). The outer crater has two peaks higher than the rest of the undamged sample, which similar to spot 12 in figure 19. Furthermore, the inner crater has increasing height towards the center of the crater. Although no cause for these heights can be concluded in this report, it could be speculated that for spot 18, that the 2 outer peaks from the outer crater correspond to those formed at lower fluence such as at spot 12.

Another interesting observation comes from noticing the depths of the craters. Not all of the Si$_y$N$_x$ is removed since only 60nm is removed (from the 121nm Si$_y$N$_x$ and 18nm SiO$_2$). Nothing can be concluded, but this could imply that the dominant damage mechanism is no longer formation microstructural changes in the Si substrate, but ablation in the Si$_y$N$_x$ itself. Reason being that if the Si substrate were responsible for damage, damage would start at the bottom. This would lead to complete material removal once damage from the bottom reaches the top of the layer. However, material is removed only at the top, meaning that there's likely no exposed Si, and ablation due to Si substrate is thus unlikely.

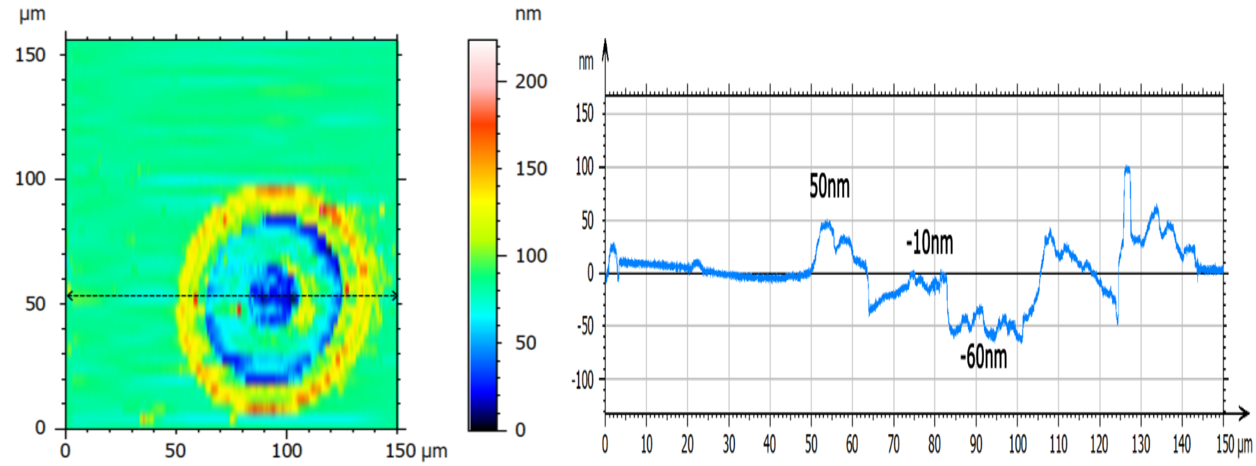

(a) Spot 18 height scan

(b) Spot 18 height profile

Figure 21: a) Height scans of Si-SiO$_2$-Si$_y$N$_x$ sample is obtained with Profilometer at spot 18. b) height profile at the cross section indicated with black stripes in a). The peaks have approximately a height of 85nm and the center 35nm with respect to the non-ablated parts.

6 Conclusion

In this report, damage mechanisms of two samples with different material compositions and thicknesses have been analyzed for single-shot, 400 nm central wavelength, pump pulses with varying fluences. Namely Si-Si$_y$N$_x$ (thin Si$_y$N$_x$ layer) and Si-SiO$_2$-Si$_y$N$_x$ (thick Si$_y$N$_x$ with 18nm SiO$_2$).

6.1 Si-Si$_y$N$_x$ sample

For the Si-Si$_y$N$_x$, it's been shown that multiple damage regimes appears for increasing pulse fluence. For pulses lower than the ablation threshold, reflectivity increases and changes below the Si$_x$N$_x$ layer which likely correspond to crystal/amorphous phase change are observed. It's also shown that those changes probably don't correspond to an "air bubble" by comparing the measured reflectence spectra with Fresnel Tranfer Matrix method calculations..

For pulses where ablation starts, AFM shows that all of the Si$_y$N$_x$ should be delaminated by height comparison (of delaminated and non-delaminted sites). Furthermore, SEM provides a strong indication that microstructural changes on the Si substrate play a role in the delamination process. These microstructural changes are also observed before ablation, as well as outside the delaminated zones, and underneath the partially delaminated Si$_y$N$_x$.

For pulses the above ablation threshold, many damage regimes with different morphology are identified with AFM and other microscopy methods. AFM shows that "pits" start appearing, where Si is removed locally. Also, Si seems to be removed over the entire delaminated spot. Some regimes have more Si removed, some have different AFM phase (compared to different damage regions), and some have increasing height near the edges.

6.2 Si-SiO$_2$-Si$_y$N$_x$ sample

For the Si-SiO$_2$-Si$_y$N$_x$ sample at fluences below ablation, changes similar to those of Si-Si$_y$N$_x$ are observed. For pulses near ablation, morphology of bulging and "donuts" (circular areas where height increases at the edges) is shown. For pulses above ablation threshold, two cascading craters can be seen, where ablation does not seem start from the Si substrate, as is likely the case Si-Si$_y$N$_x$ sample.

6.3 Outlook

This report has found different damage regions and corresponding fluence thresholds for Si-Si$_y$N$_x$ and Si-SiO$_2$-Si$_y$N$_x$ samples. The next step would be to define the ablation mechanisms. Firstly, the amount of data should be increased by repeating the experiment. This implies damaging more samples, and repeat all of characterization done is this report, but for more fluences. However, this likely won't give concrete evidence on mechanisms such as phase change. For that reason, it would be interesting to use Raman Spectroscopy or Electron Backscatter Diffraction to identify material phases in each region as implemented in literature [23, 26, 41]

Another suggestion would be to cut the sample with an Focused Ion Beam, and use Transmission Electron Microscopy to image the microstructural changes and the edges of each regime. It would also be usefull to use Energy-Dispersive X-ray spectroscopy to gain an idea of material composition, as this could give insights if there's diffusion or partial delamination. Lastly, measurements of samples with varying thicknesses can give leads on damage mechanisms, as it's seen that the dominating damage mechanisms could depend on thickness by seeing different damage in Si-Si$_y$N$_x$ and Si-SiO$_2$-Si$_y$N$_x$ samples. This could also be explained by the presence of SiO$_2$ however, and should thus also be verified removing the SiO$_2$ layer and checking if the damage changes.

References

[1] D. J. Moss, R. Morandotti, A. L. Gaeta, and M. Lipson, "New CMOS-compatible platforms based on silicon nitride and Hydex for nonlinear optics," *Nature Photonics 2013 7:8*, vol. 7, no. 8, pp. 597–607, 7 2013. [Online]. Available: https://www.nature.com/articles/nphoton.2013.183

[2] J. Feldmann, N. Youngblood, M. Karpov, H. Gehring, X. Li, M. Stappers, M. Le Gallo, X. Fu, A. Lukashchuk, A. S. Raja, J. Liu, C. D. Wright, A. Sebastian, T. J. Kippenberg, W. H. Pernice, and H. Bhaskaran, "Parallel convolutional processing using an integrated photonic tensor core," *Nature 2020 589:7840*, vol. 589, no. 7840, pp. 52–58, 1 2021. [Online]. Available: https://www.nature.com/articles/s41586-020-03070-1

[3] D. J. Blumenthal, R. Heideman, D. Geuzebroek, A. Leinse, and C. Roeloffzen, "Silicon Nitride in Silicon Photonics," *Proceedings of the IEEE*, vol. 106, no. 12, pp. 2209–2231, 12 2018.

[4] K. Wörhoff, R. G. Heideman, A. Leinse, and M. Hoekman, "TriPleX: A versatile dielectric photonic platform," *Advanced Optical Technologies*, vol. 4, no. 2, pp. 189–207, 4 2015. [Online]. Available: https://www.degruyter.com/document/doi/10.1515/aot-2015-0016/html

[5] J. Schmidt, R. Peibst, and R. Brendel, "Surface passivation of crystalline silicon solar cells: Present and future," *Solar Energy Materials and Solar Cells*, vol. 187, pp. 39–54, 12 2018.

[6] E. Franklin, K. Fong, K. McIntosh, A. Fell, A. Blakers, T. Kho, D. Walter, D. Wang, N. Zin, M. Stocks, E. C. Wang, N. Grant, Y. Wan, Y. Yang, X. Zhang, Z. Feng, and P. J. Verlinden, "Design, fabrication and characterisation of a 24.4% efficient interdigitated back contact solar cell," *Progress in Photovoltaics: Research and Applications*, vol. 24, no. 4, pp. 411–427, 4 2016. [Online]. Available: https://onlinelibrary.wiley.com/doi/full/10.1002/pip.2556https://onlinelibrary.wiley.com/doi/abs/10.1002/pip.2556https://onlinelibrary.wiley.com/doi/10.1002/pip.2556

[7] R. Bhatt, I. Kravchenko, and M. Gupta, "High-efficiency solar thermophotovoltaic system using a nanostructure-based selective emitter," *Solar Energy*, vol. 197, pp. 538–545, 2 2020.

[8] Y. Yang, J. Kuang, H. Wang, G. Song, Y. Liu, and G. Tang, "Enhancement in thermal property of phase change microcapsules with modified silicon nitride for solar energy," *Solar Energy Materials and Solar Cells*, vol. 151, pp. 89–95, 7 2016.

[9] F. Krach, H. Schwarzmann, A. J. Bauer, T. Erlbacher, and L. Frey, "Silicon nitride, a high potential dielectric for 600 V integrated RC-snubber applications," *Journal of Vacuum Science & Technology B, Nanotechnology and Microelectronics: Materials, Processing, Measurement, and Phenomena*, vol. 33, no. 1, p. 01A112, 1 2015. [Online]. Available: /avs/jvb/article/33/1/01A112/590959/Silicon-nitride-a-high-potential-dielectric-for

[10] O. Richard, S. Blais, R. Arès, V. Aimez, and A. Jaouad, "Mechanisms of GaAs surface passivation by a one-step dry process using low-frequency plasma enhanced chemical deposition of silicon nitride," *Microelectronic Engineering*, vol. 233, p. 111398, 9 2020.

[11] P. Divya, A. Kumar, and W. H. Lee, "Effects of SiNX passivation on GaN-HEMT DC characteristics," *Materials Science in Semiconductor Processing*, vol. 148, p. 106716, 9 2022.

[12] K. Lee, S. Kim, G. Lee, S. Lee, J. Cho, W. Kim, C. Bok, H. Kim, S. Moon, and J. Kim, "Development of multi-function hard mask to simplify process step," *https://doi.org/10.1117/12.656870*, vol. 6153, pp. 898–905, 4 2006. [Online]. Available: https://www.spiedigitallibrary.org/conference-proceedings-of-spie/6153/61532V/Development-of-multi-function-hard-mask-to-simplify-process-step/10.1117/12.656870.fullhttps://www.spiedigitallibrary.org/conference-proceedings-of-spie/6153/61532V/Development-of-multi-function-hard-mask-to-simplify-process-step/10.1117/12.656870.short

[13] S. Shi, X. Wang, C. Xu, J. Yuan, J. Fang, S. Jiang, and S. Liu, "Fabricating processes of free-standing silicon nitride thin film for MEMS devices," *Proceedings - 2013 14th International Conference on Electronic Packaging Technology, ICEPT 2013*, pp. 23–26, 2013.

[14] H. J. M. Veendrick, "Manufacture of MOS Devices," *Nanometer CMOS ICs*, pp. 73–159, 2017. [Online]. Available: https://link.springer.com/chapter/10.1007/978-3-319-47597-4_3

[15] H. H. Radamson, H. Zhu, Z. Wu, X. He, H. Lin, J. Liu, J. Xiang, Z. Kong, W. Xiong, J. Li, H. Cui, J. Gao, H. Yang, Y. Du, B. Xu, B. Li, X. Zhao, J. Yu, Y. Dong, and G. Wang, "State of the Art and Future Perspectives in Advanced CMOS Technology," *Nanomaterials 2020, Vol. 10, Page 1555*, vol. 10, no. 8, p. 1555, 8 2020. [Online]. Available: https://www.mdpi.com/2079-4991/10/8/1555/htmhttps://www.mdpi.com/2079-4991/10/8/1555

[16] G. Heinrich, I. Höger, M. Bähr, K. Stolberg, T. Wütherich, M. Leonhardt, A. Lawerenz, and G. Gobsch, "Investigation of Laser Irradiated Areas with Electron Backscatter Diffraction," *Energy Procedia*, vol. 27, pp. 491–496, 1 2012.

[17] X. Yu, L. Jiang, Q. Luan, Y. Cai, Q. Song, B. Wang, and Z. Liu, "Investigation of mechanism and surface morphology on the femtosecond laser ablation of silicon nitride under different auxiliary processing environments," *Ceramics International*, vol. 49, no. 9, pp. 13 425–13 434, 5 2023.

[18] S. Nevarez, C. M. Stewart, C. Yirong Lin, R. Grodsky, and B. L. Stephen Crites, "FEMTOSECOND LASER MACHINING OF DRILLED HOLES IN SILICON NITRIDE."

[19] G. Heinrich and A. Lawerenz, "Non-linear absorption of femtosecond laser pulses in a SiNx layer—influence of silicon doping type," *Solar Energy Materials and Solar Cells*, vol. 120, no. PART A, pp. 317–322, 1 2014.

[20] S. Rapp, G. Heinrich, M. Domke, and H. P. Huber, "The Combination of Direct and Confined Laser Ablation Mechanisms for the Selective Structuring of Thin Silicon Nitride Layers," *Physics Procedia*, vol. 56, no. C, pp. 998–1006, 1 2014.

[21] S. Rapp, M. Schmidt, and H. P. Huber, "Selective femtosecond laser structuring of dielectric thin films with different band gaps: a time-resolved study of ablation mechanisms," *Applied Physics A: Materials Science and Processing*, vol. 122, no. 12, pp. 1–13, 12 2016. [Online]. Available: https://link.springer.com/article/10.1007/s00339-016-0571-0

[22] S. Bashir, M. Shahid Rafique, and W. Husinsky, "Identification of ultra-fast electronic and thermal processes during femtosecond laser ablation of Si," *Applied Physics A: Materials Science and Processing*, vol. 109, no. 2, pp. 421–429, 11 2012. [Online]. Available: https://link.springer.com/article/10.1007/s00339-012-7067-3

[23] M. J. Smith, M. J. Sher, B. Franta, Y. T. Lin, E. Mazur, and S. Gradečak, "The origins of pressure-induced phase transformations during the surface texturing of silicon using femtosecond laser irradiation," *Journal of Applied Physics*, vol. 112, no. 8, 10 2012. [Online]. Available: /aip/jap/article/112/8/083518/375719/The-origins-of-pressure-induced-phase

[24] "Ultra-short laser ablation of metals and semiconductors: evidence of ultra-fast Coulomb explosion."

[25] A. Mené Ndez-Manjo´n, M. Manjo´n, S. Barcikowski, G. A. Shafeev, V. I. Mazhukin, Chichkov, and B. N, "Influence of beam intensity profile on the aerodynamic particle size distributions generated by femtosecond laser ablation." [Online]. Available: https://doi.org/10.1017/S0263034609990553

[26] K. Werner, V. Gruzdev, N. Talisa, K. Kafka, D. Austin, C. M. Liebig, and E. Chowdhury, "Single-Shot Multi-Stage Damage and Ablation of Silicon by Femtosecond Mid-infrared Laser Pulses," *Scientific Reports 2019 9:1*, vol. 9, no. 1, pp. 1–13, 12 2019. [Online]. Available: https://www.nature.com/articles/s41598-019-56384-0

[27] R. Le Harzic, H. Schuck, D. Sauer, T. Anhut, I. Riemann, K. König, J. Pedraza, J. D. Fowlkes, D. H. Lowndes, N. Bärsch, K. Körber, A. Ostendorf, C. H. Crouch, J. E. Carey, J. M. Warrender, M. J. Aziz, E. Mazur, and F. Y. Génin, "Sub-100 nm nanostructuring of silicon by ultrashort laser pulses," *Optics Express, Vol. 13, Issue 17, pp. 6651-6656*, vol. 13, no. 17, pp. 6651–6656, 8 2005. [Online]. Available: https://opg.optica.org/viewmedia.cfm?uri=oe-13-17-6651&seq=0&html=truehttps://opg.optica.org/abstract.cfm?uri=oe-13-17-6651https://opg.optica.org/oe/abstract.cfm?uri=oe-13-17-6651

[28] X. J. Zeng, X. Mao, R. Greif, and R. E. Russo, "Ultraviolet femtosecond and nanosecond laser ablation of silicon: ablation efficiency and laser-induced plasma expansion," *https://doi.org/10.1117/12.544401*, vol. 5448, pp. 1150–1158, 9 2004. [Online]. Available: https://www.spiedigitallibrary.org/conference-proceedings-of-spie/5448/0000/Ultraviolet-femtosecond-and-nanosecond-laser-ablation-of-silicon--ablation/10.1117/12.544401.fullhttps://www.spiedigitallibrary.org/conference-proceedings-of-spie/5448/0000/Ultraviolet-femtosecond-and-nanosecond-laser-ablation-of-silicon--ablation/10.1117/12.544401.short

[29] H. Dachraoui and W. Husinsky, "Thresholds of Plasma Formation in Silicon Identified by Optimizing the Ablation Laser Pulse Form," 2006.

[30] J. M. Liu, "Simple technique for measurements of pulsed Gaussian-beam spot sizes," *Optics Letters, Vol. 7, Issue 5, pp. 196-198*, vol. 7, no. 5, pp. 196–198, 5 1982. [Online]. Available: https://opg.optica.org/viewmedia.cfm?uri=ol-7-5-196&seq=0&html=truehttps://opg.optica.org/abstract.cfm?uri=ol-7-5-196https://opg.optica.org/ol/abstract.cfm?uri=ol-7-5-196

[31] E. Abram, I. Milov, N. Orlov, K. Van Druten, E. Garnett, and P. Planken, "Pre-ablation regime light-induced optical changes in nanometer thick metal films," *Manuscript in preparation*, 2023.

[32] M. B. Helmes, "Surface passivation of germanium by PECVD of SiNx."

[33] C. Florian, D. Fischer, K. Freiberg, M. Duwe, M. Sahre, S. Schneider, A. Hertwig, J. Krüger, M. Rettenmayr, U. Beck, A. Undisz, and J. Bonse, "Single Femtosecond Laser-Pulse-Induced Superficial Amorphization and Re-Crystallization of Silicon," *Materials 2021, Vol. 14, Page 1651*, vol. 14, no. 7, p. 1651, 3 2021. [Online]. Available: https://www.mdpi.com/1996-1944/14/7/1651/htmhttps://www.mdpi.com/1996-1944/14/7/1651

[34] S. Adachi and H. Mori, "Optical properties of fully amorphous silicon."

[35] e. Burstein, J. J. Oberly, and J. W. Davisson, "INF LUENC E OF PHONONS ON THE."

[36] M. A. Green, "Self-consistent optical parameters of intrinsic silicon at 300 K including temperature coefficients," *Solar Energy Materials and Solar Cells*, vol. 92, no. 11, pp. 1305–1310, 11 2008.

[37] S. J. Byrnes, "Multilayer optical calculations," 2020. [Online]. Available: https://pypi.python.org/pypi/tmm.

[38] H. Daido, M. Nishiuchi, and A. S. Pirozhkov, "Coulomb explosion and early plasma generation during femtosecond laser ablation of silicon at high laser fluence," *J. Phys. D: Appl. Phys*, vol. 46, p. 335501, 2013.

[39] J. Bonse, S. Baudach, J. Krüger, W. Kautek, and M. Lenzner, "Femtosecond laser ablation of silicon-modification thresholds and morphology," *Appl. Phys. A*, vol. 74, pp. 19–25, 2002.

[40] D. Hu, Y. Lu, Y. Cao, Y. Zhang, Y. Xu, W. Li, F. Gao, B. Cai, B. O. Guan, C. W. Qiu, and X. Li, "Laser-Splashed Three-Dimensional Plasmonic Nanovolcanoes for Steganography in Angular Anisotropy," *ACS Nano*, vol. 12, no. 9, pp. 9233–9239, 9 2018. [Online]. Available: https://pubs.acs.org/doi/full/10.1021/acsnano.8b03964

[41] J. Bonse, K. W. Brzezinka, and A. J. Meixner, "Modifying single-crystalline silicon by femtosecond laser pulses: an analysis by micro Raman spectroscopy, scanning laser microscopy and atomic force microscopy," *Applied Surface Science*, vol. 221, no. 1-4, pp. 215–230, 1 2004.

[42] G. D. Tsibidis, M. Barberoglou, P. A. Loukakos, E. Stratakis, and C. Fotakis, "Dynamics of ripple formation on silicon surfaces by ultrashort laser pulses in subablation conditions," *PHYSICAL REVIEW B*, vol. 86, p. 115316, 2012.

A Appendix

A.1 Dark Field and Bright Field Microscopy

Some images have been compressed. This is indicated i the caption.

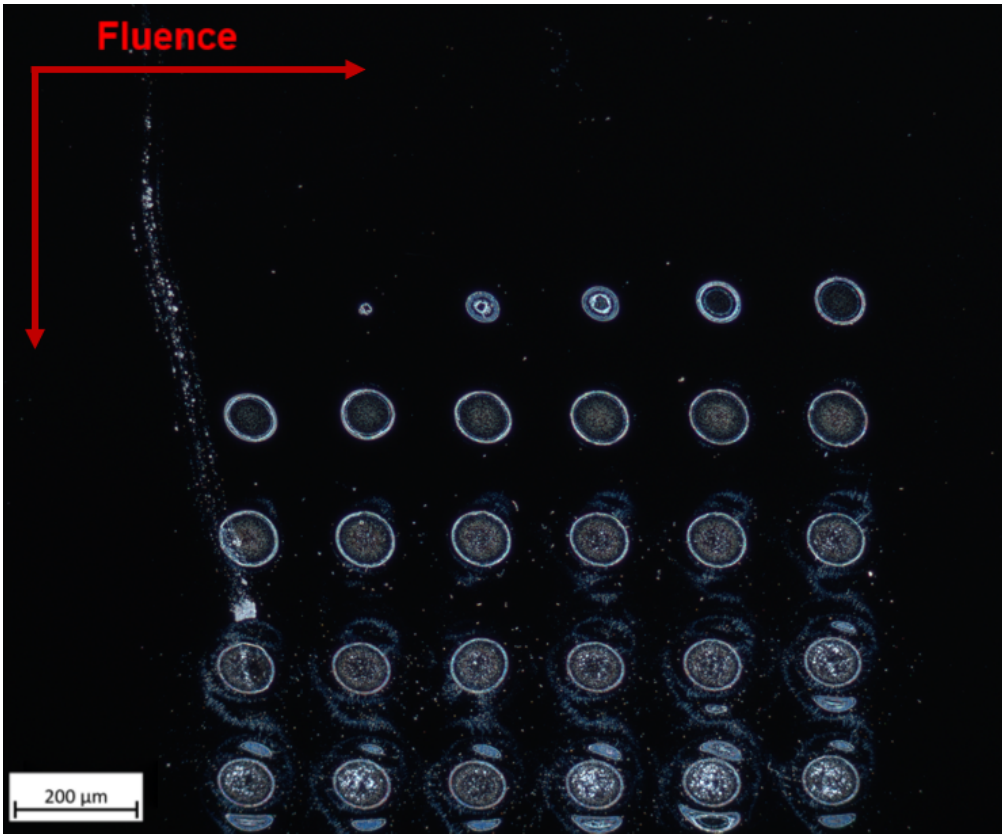

Figure 22: Figure of Dark Field Microscope of Si-Si$_y$N$_x$ before cleaning with water and isopropanol in an ultrasound bath.

A.2 Liu analysis

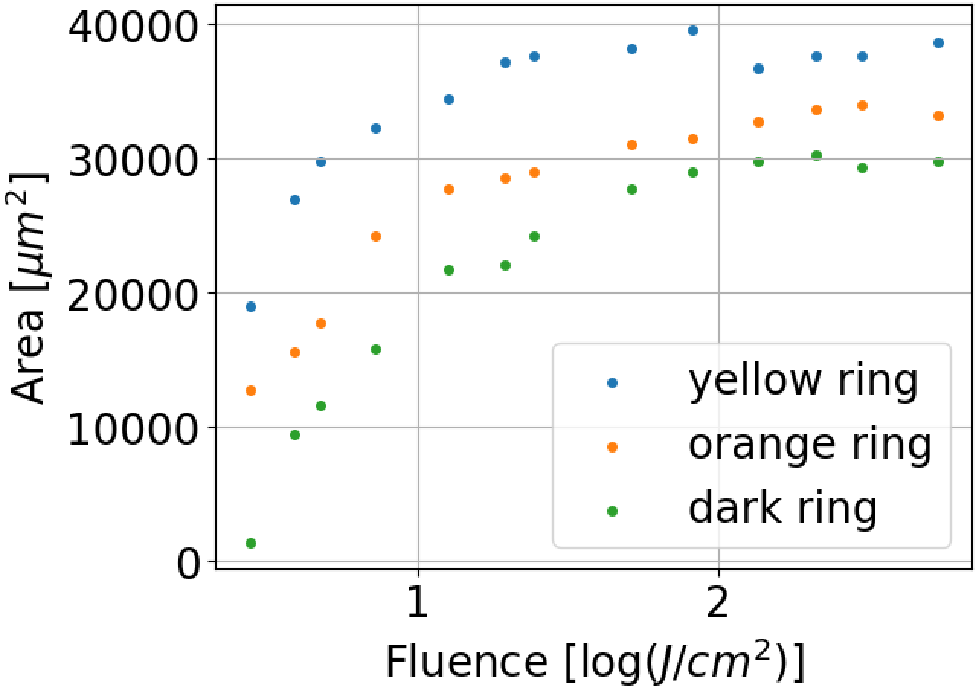

Figure 23: Plot of area (yellow, orange and dark areas visible in figure 4 used), against fluence in logarithmic scale for Si-Si$_y$N$_x$ sample. Only the first 4 data points are used for fitting to maintain linearity.

A.3 Ellipsometry

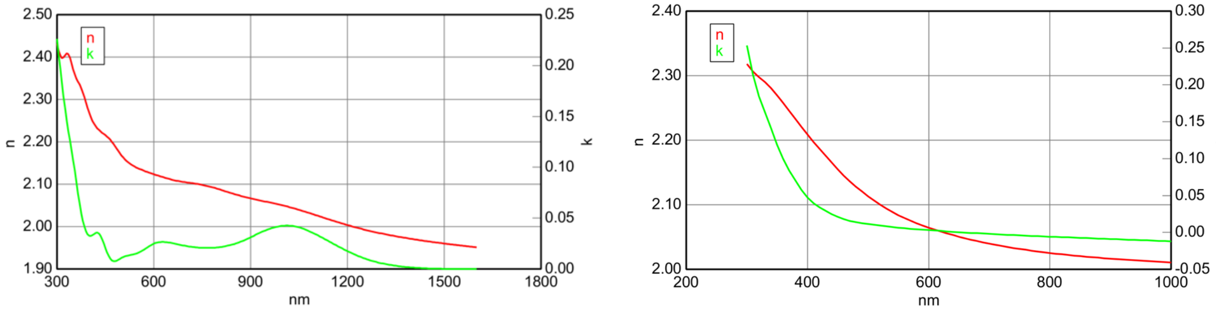

(a) Si-Si$_y$N$_x$ sample

(b) Si-SiO$_2$-Si$_y$N$_x$ sample

Figure 24: Figure of n and k refractive indices after ellipsometry fit for Si-Si$_y$N$_x$ and Si-SiO$_2$-Si$_y$N$_x$ sample, giving a bandgap at 400nm (3.1eV)

A.4 Reflectance microscopy

Reflectance microscope had issues regarding calibration.

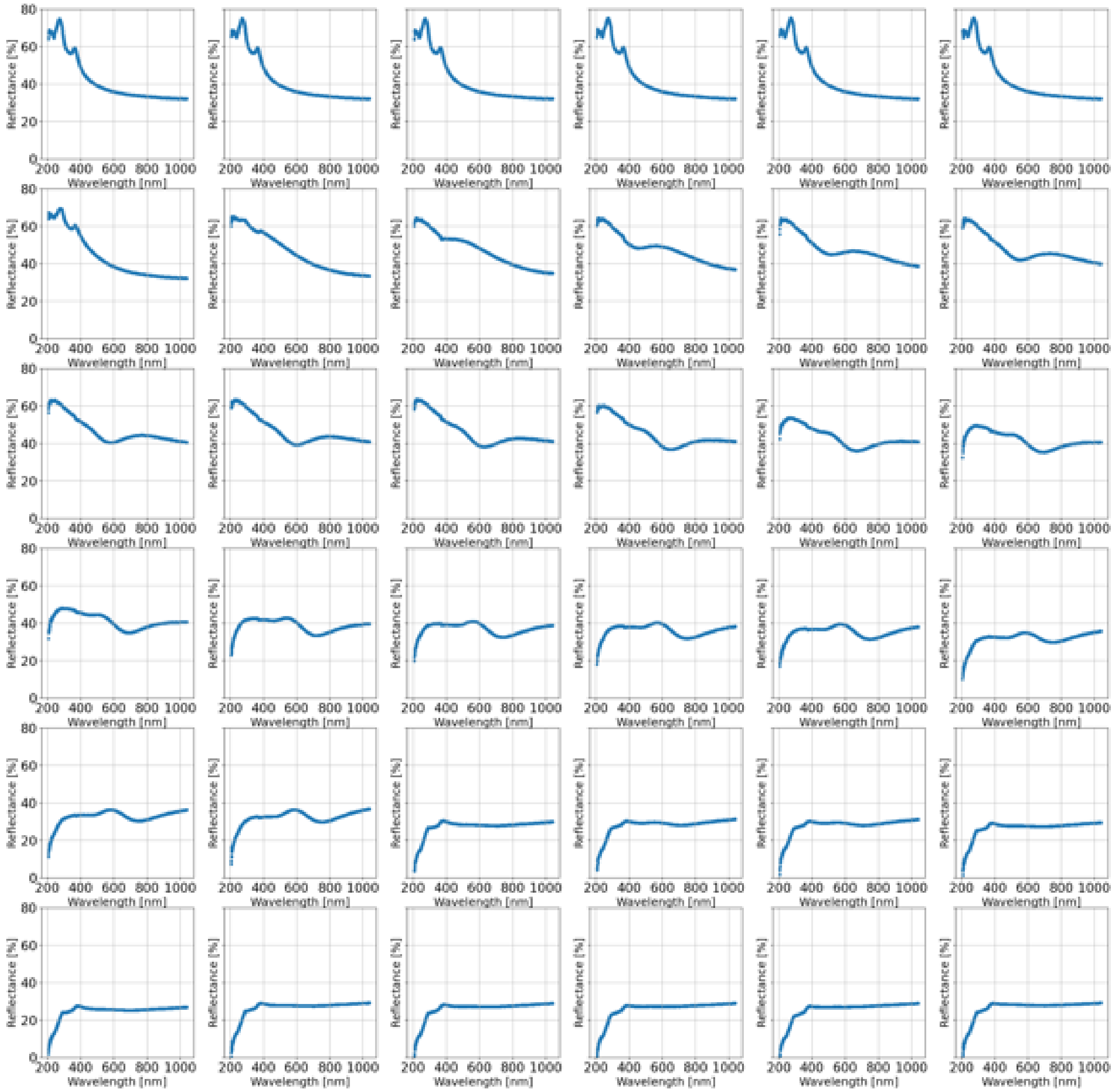

Figure 25: Reflectance spectra of Si for increasing fluence. The figure is made by averaging 3 grids.

Spot	**Variance (Si-Si$_y$N$_x$)**	**Variance (Si-Si$_y$N$_x$)**
1	80.8460	168.2195
2	81.0475	168.3271
3	81.0614	168.3933
4	81.3214	168.3350
5	90.0295	168.3913
6	155.1589	168.3377
7	189.1782	168.3902
8	57.6562	169.3209
9	22.3611	178.1218
10	9.60417	205.8777
11	14.8906	249.3485
12	19.6944	288.2768
13	30.7765	239.9356
14	32.6172	64.9783
15	28.0932	95.7614
16	28.6017	96.0745
17	26.9042	109.9184
18	28.4300	141.6214
19	26.3534	161.3177
20	19.9987	162.7010
21	17.3837	156.1976
22	15.5713	149.0463
23	10.8648	136.7249
24	11.4717	132.0342
25	12.3697	127.3966
26	9.8430	128.4364
27	8.0626	130.8093
28	9.5170	131.1232
29	7.8800	132.6943
30	8.9197	131.3318
31	9.0609	131.7320
32	9.1859	133.2663
33	9.4006	118.1263
34	4.9251	132.9435
35	8.4423	131.6282
36	8.8724	129.0499

Table 3: Table variances of figure 5 and 8 for Si-Si$_y$N$_x$ sample and Si-SiO$_2$-Si$_y$N$_x$ sample

A.5 Multilayer simulations

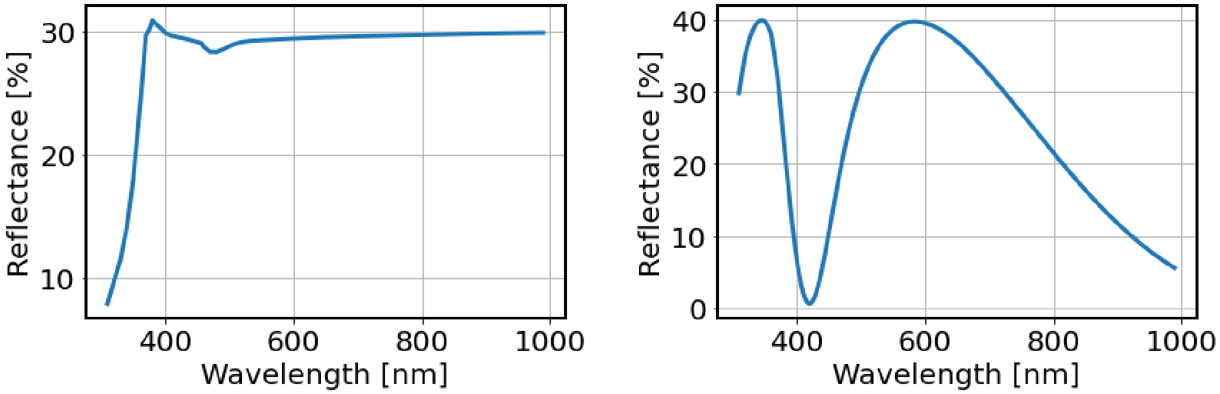

(a) Si-Si$_y$N$_x$

(b) Si-SiO$_2$-Si$_y$N$_x$

Figure 26: Multilayer simulation of reflectance against incident wavelength for Si-Si$_y$N$_x$ and Si-SiO$_2$-Si$_y$N$_x$ samples.

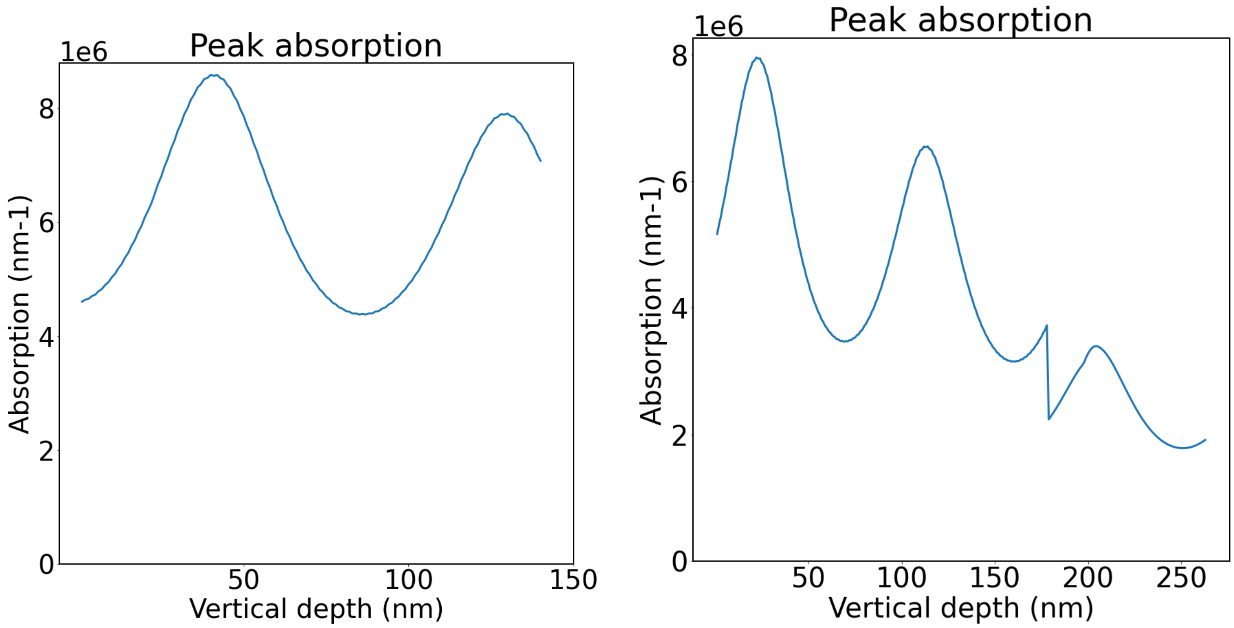

(a) Si-Si$_y$N$_x$

(b) Si-SiO$_2$-Si$_y$N$_x$

Figure 27: Multilayer simulation of absorption profle against depth in sample for Si-Si$_y$N$_x$ and Si-SiO$_2$-Si$_y$N$_x$ samples. For example, in Si-Si$_y$N$_x$, first 21nm are Si$_y$N$_x$, after that there's the native Si, and then Si substrate. Used depths are indicated with ellipsometry 4.3.5

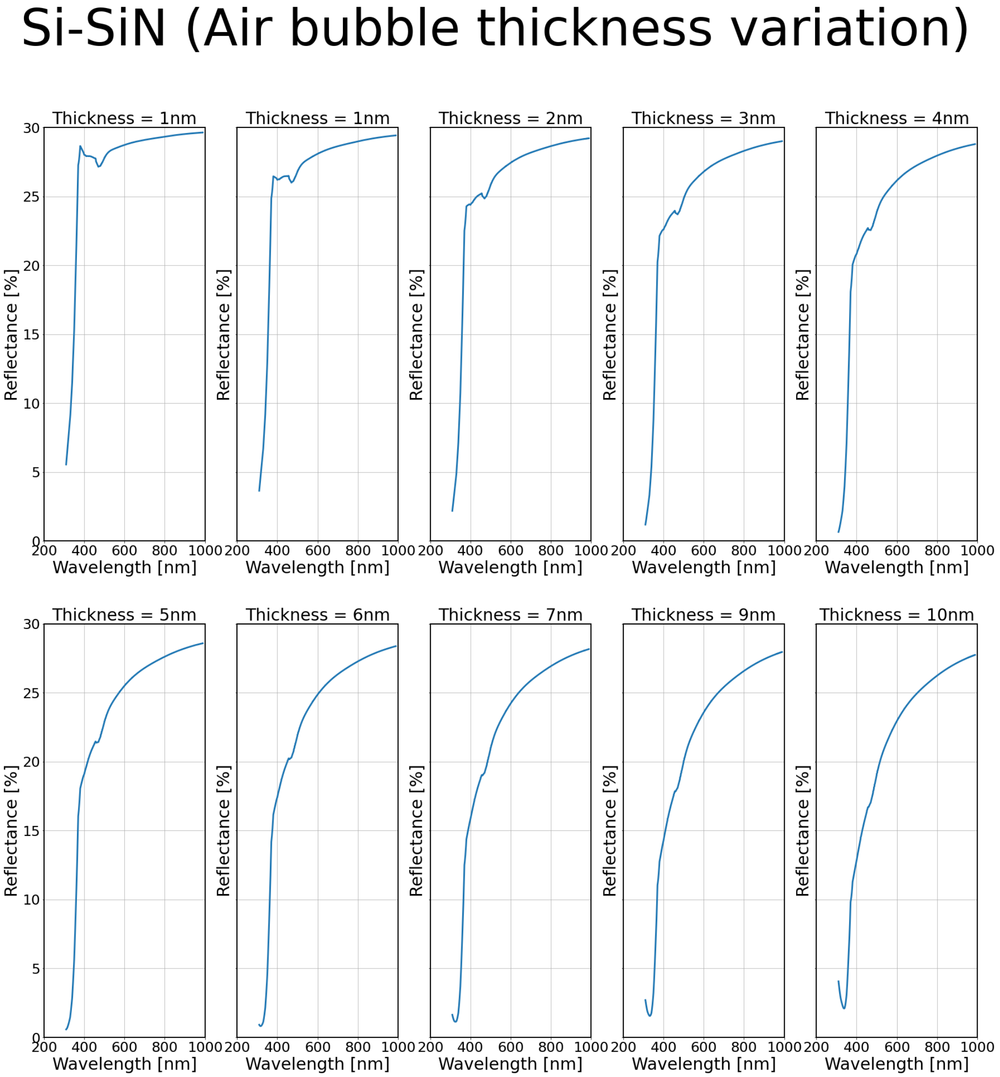

Figure 28: Multilayer simulation Si-Si$_y$N$_x$ sample adding an "air bubble" (hollow in layer in between Si$_y$N$_x$ and Si$_{native}$). Reflectance spectra is shown for different "air bubble" thicknesses.

A.6 Scanning Electron Microscopy

All images used in this report for SEM have been compressed, meaning that if zoom in is done on any of the images, black spots will appear which are artifacts. This is indicated in the caption

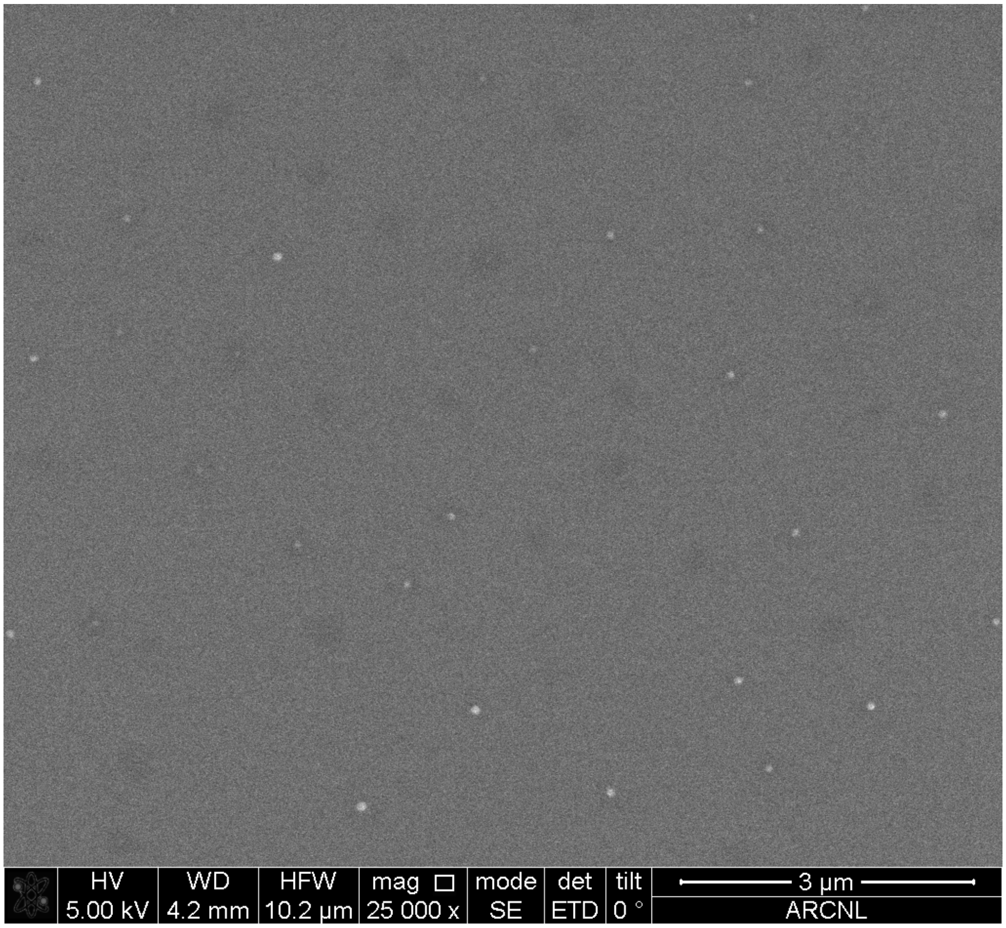

Figure 29: SEM image of a pristine site (spot where laser has not irradiated). Image was taken after performin laser measurement.

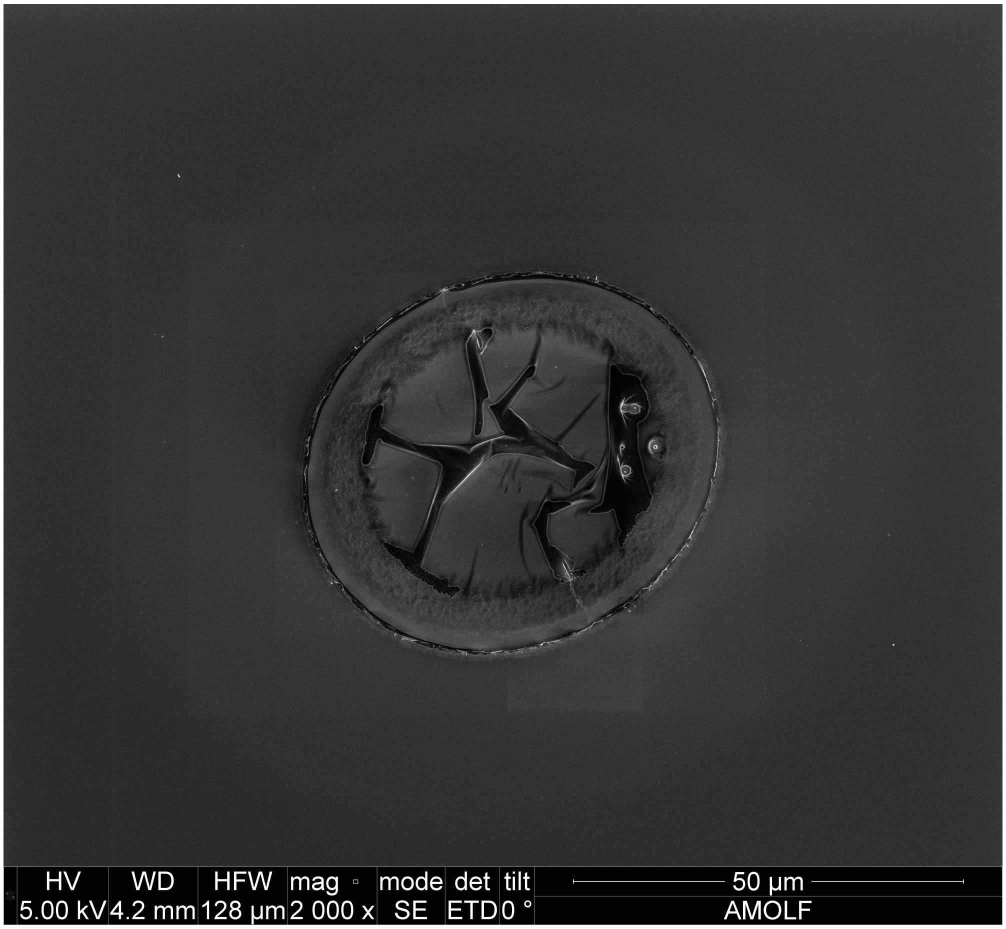

Figure 30: SEM image of an ablation spot (different grid) at $F = 0.25\frac{J}{cm^2}$.

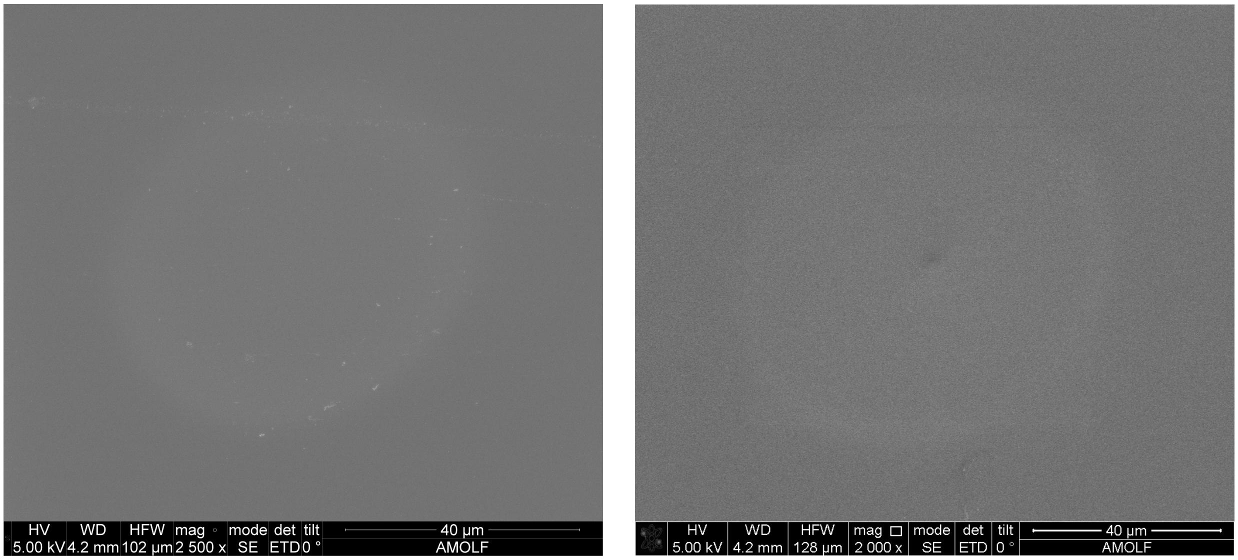

(a) Spot 6 $= 0.24\frac{J}{cm^2}$

(b) Spot 7 $= 0.34\frac{J}{cm^2}$

Figure 31: SEM of Si-Si$_y$N$_x$ of spots 6 and 7. Spots are only visible under Bright Field Microscope. b) Dark color at center in spot 7 could be due to carbon, or ablation. Image was compressed

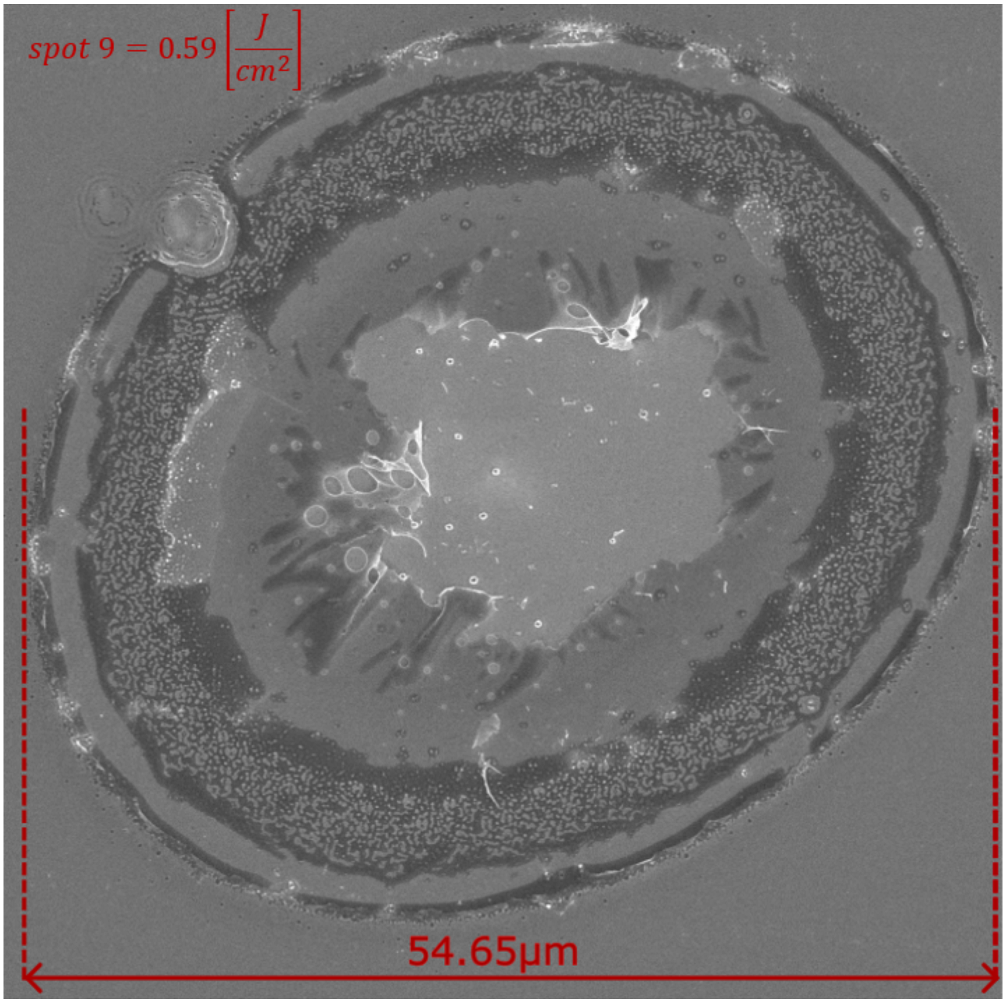

Figure 32: SEM image of an ablation spot 9 with fluence $F = 0.59 \frac{J}{cm^2}$.

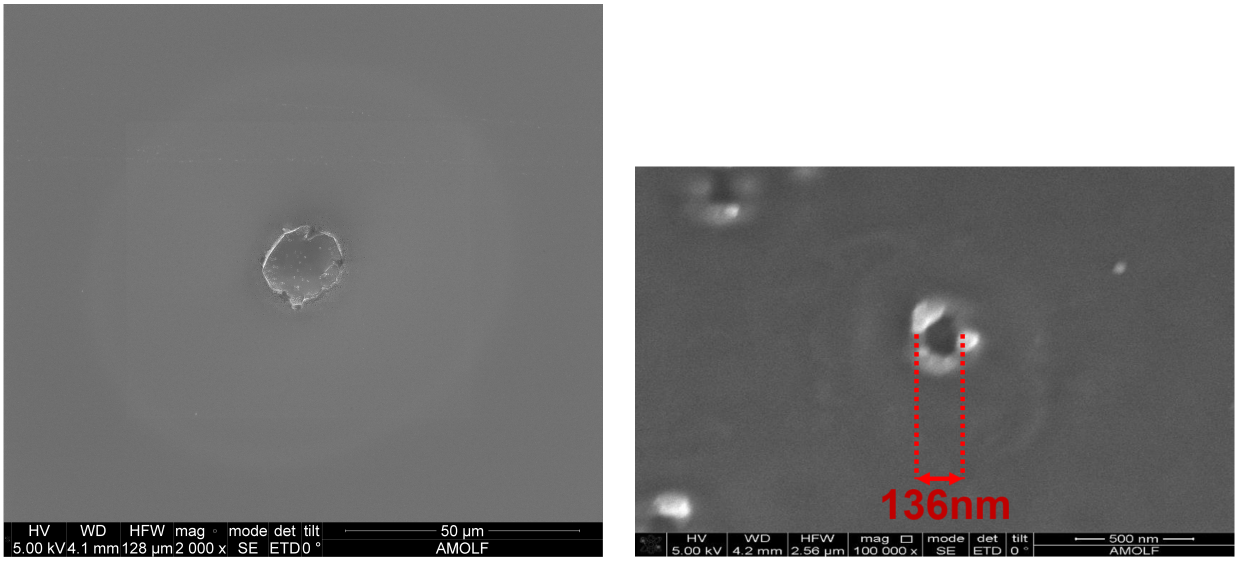

(a) SEM image of ablation spot 8 at $F = 0.44\frac{J}{cm^2}$

(b) SEM image of Spot 8 zoomed into a single nanohill.

Figure 33: a) SEM image of spot 8 at $F = 0.44\frac{J}{cm^2}$. b) zoomed in on a nanohill in the center of the delaminated area. Image was compressed

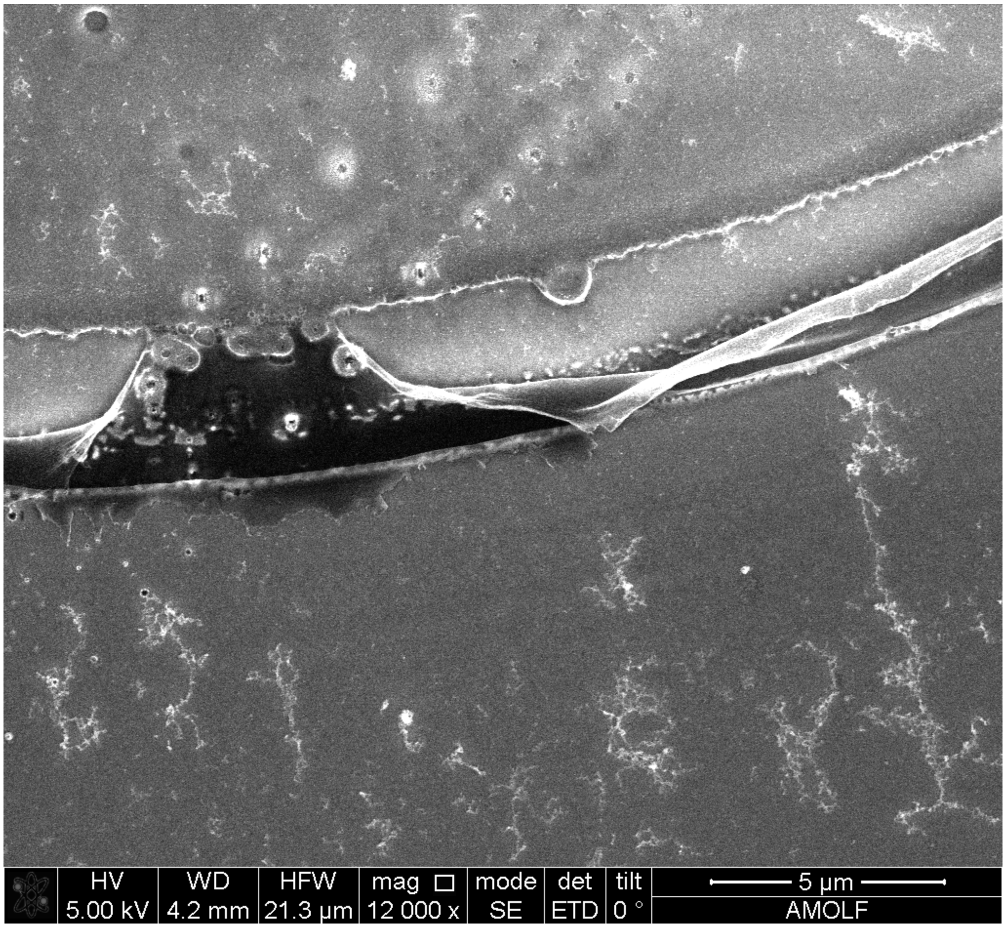

Figure 34: SEM image of the bottom edge of an ablation spot with fluence $F = 1.72\frac{J}{cm^2}$.

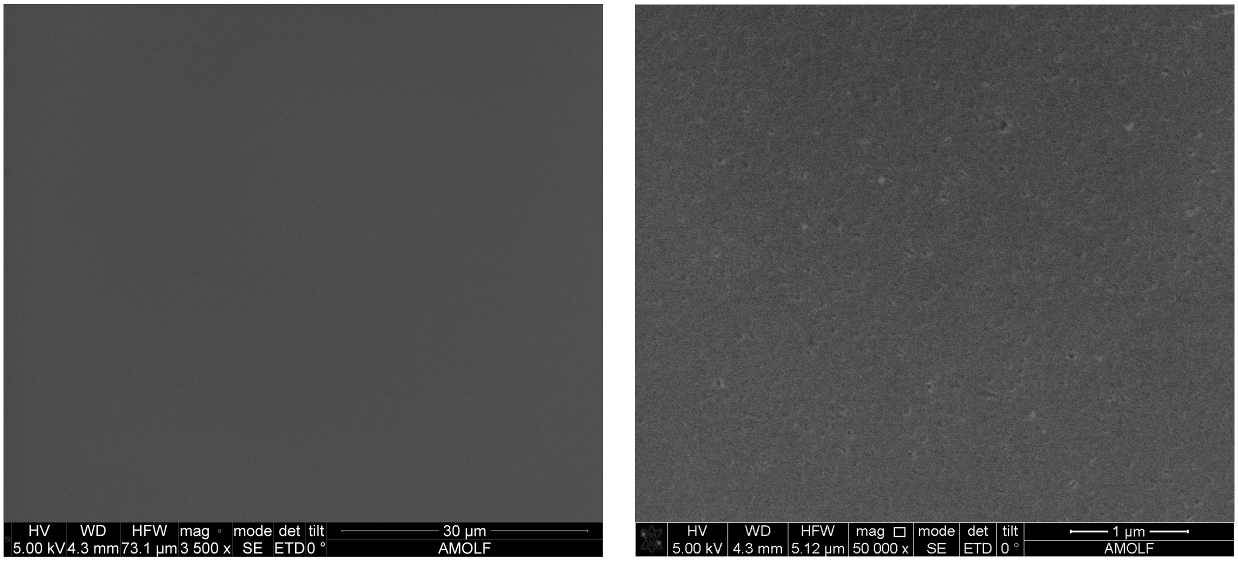

(a) Spot 6 = $0.24\frac{J}{cm^2}$

(b) Spot 7 = $0.34\frac{J}{cm^2}$

Figure 35: SEM of Si-SiO$_2$-Si$_y$N$_x$ sample of spots 10 in a) and 11 in b). a) change is not visible (possibly due to 121.3nm thickness of Si$_y$N$_x$ giving poor visibility). b) has higher magnification, which shows web-like modifications.

A.7 Atomic Force Microscopy

Spot 8 and 20 had their heights leveled with respect to non-delaminated site

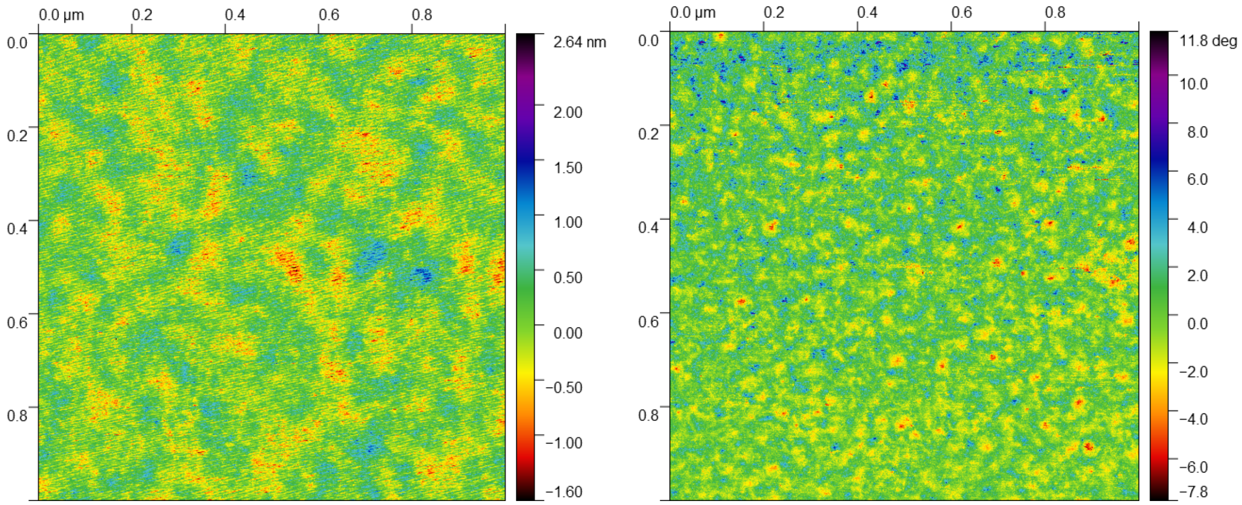

(a) Height

(b) Phase

Figure 36: AFM of Si-Si$_y$N$_x$ sample at spot 6 (center), showing a) height and b) phase.

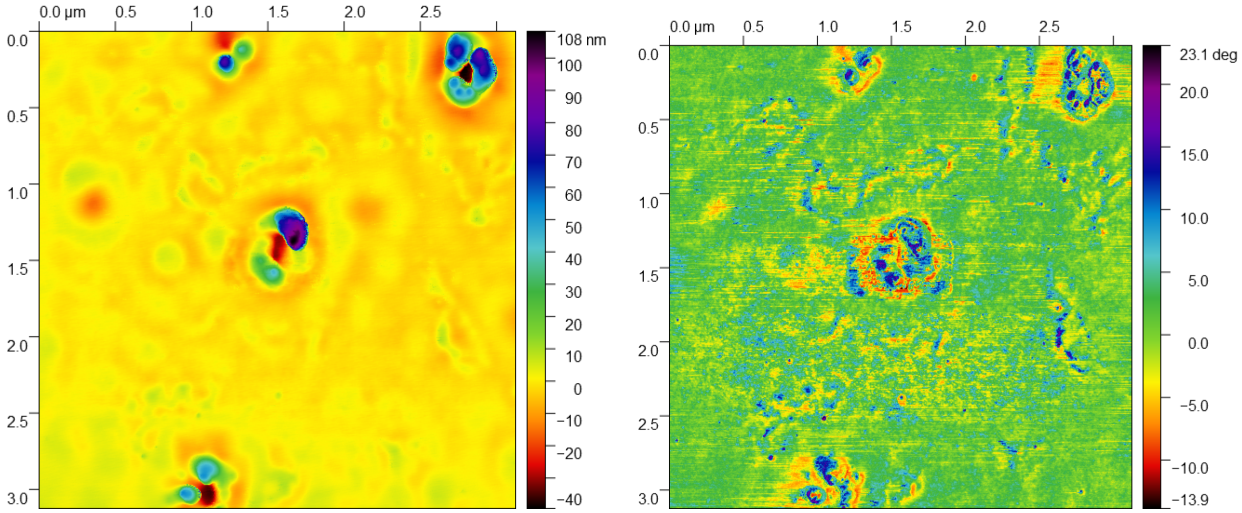

(a) Height

(b) Phase

Figure 37: AFM of Si-Si$_y$N$_x$ sample at spot 8 (center, but different spot than in figure 13), showing nanovolcanos with a) height and b) AFM phase.

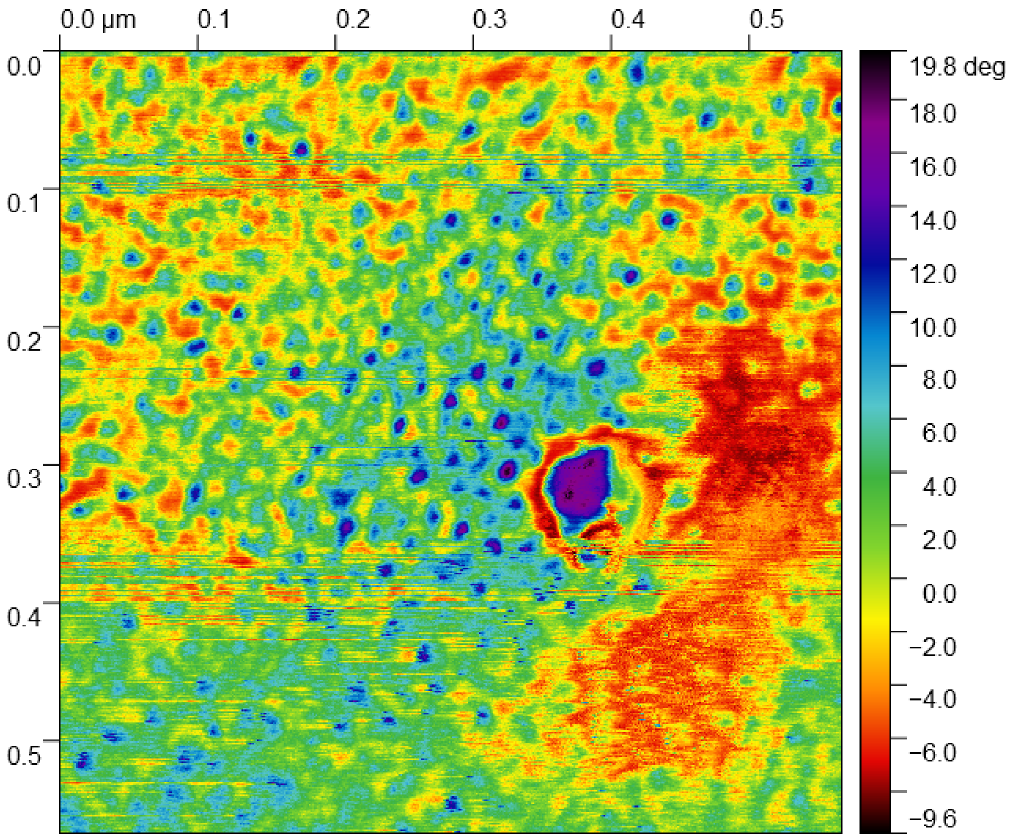

Figure 38: same scan as figure 14 (spot 8), but with only phase

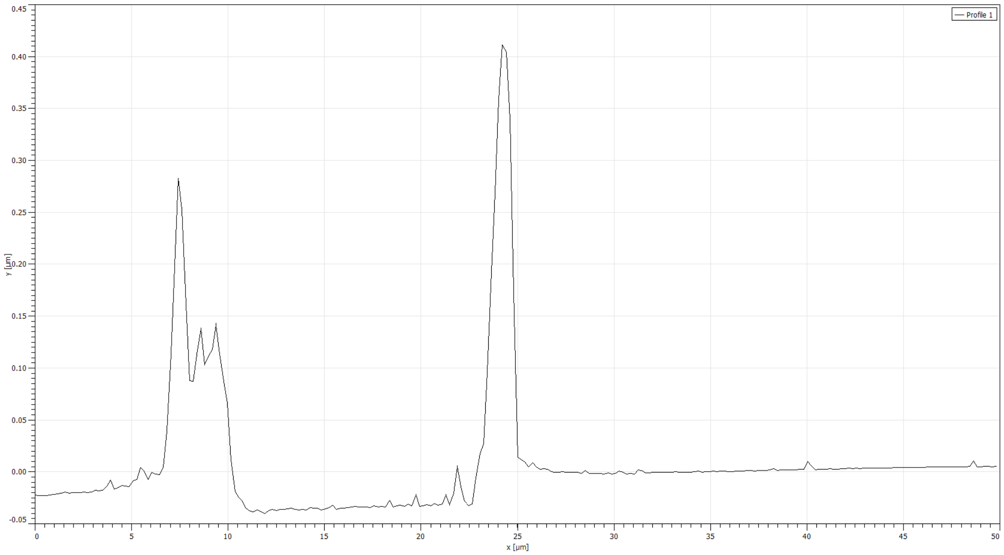

Figure 39: AFM scan of spot 8 showing horizontal height profile across the delaminated site. Height difference is approximately 22nm, which is the same amount of deposited $\mathrm{Si}_y\mathrm{N}_x$

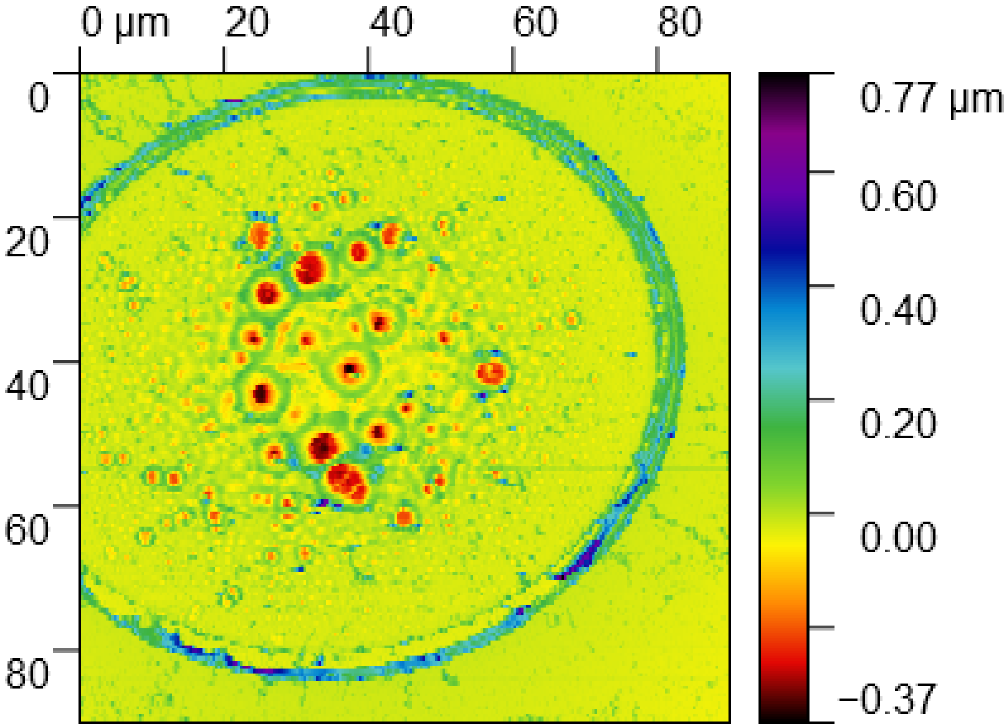

Figure 40: AFM scan of Si-$\mathrm{Si}_y\mathrm{N}_x$ sample spot 36 showing horizontal height profile.

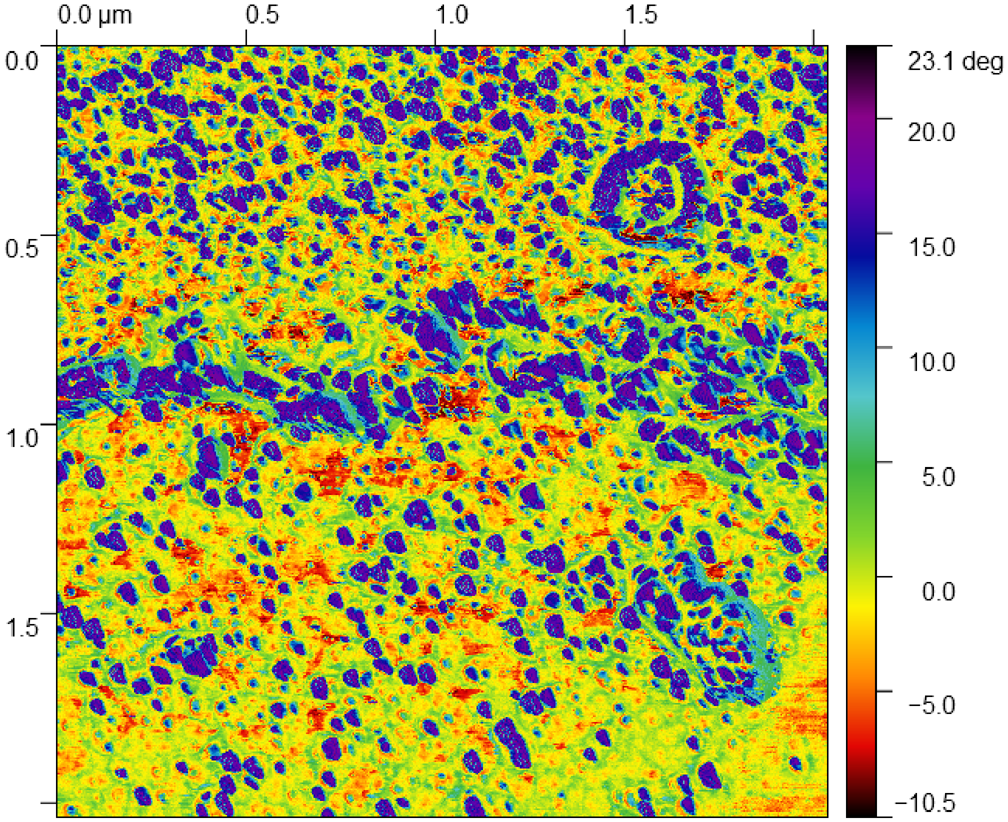

Figure 41: Same scan as figure 14 (spot 20 zoomed on region 3.1), but with only phase

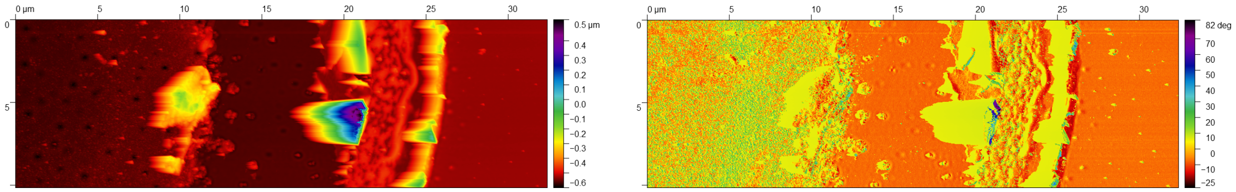

(a) Height

(b) Phase

Figure 42: AFM of Si-Si$_y$N$_x$ sample at spot 11 (right edge at regime center-2) showing a) height and b) AFM phase.

A.7.1 No Light Induced Periodic Surface Structures

For Si-SiO$_2$-Si$_y$N$_x$ sample spot 12 in SEM figure 20, horizontal stripes can be noticed. Literature does see Light Induced Periodic Surface Structures (LIPSS) in Si usually for multi-shot measurements [27]. However, the structures observed do not appear near the center of the ablation spot as evidenced by lower fluence figures and are not completely periodic as seen in figure A-43. Also, these structures are not observed at different grids for the similar fluences.

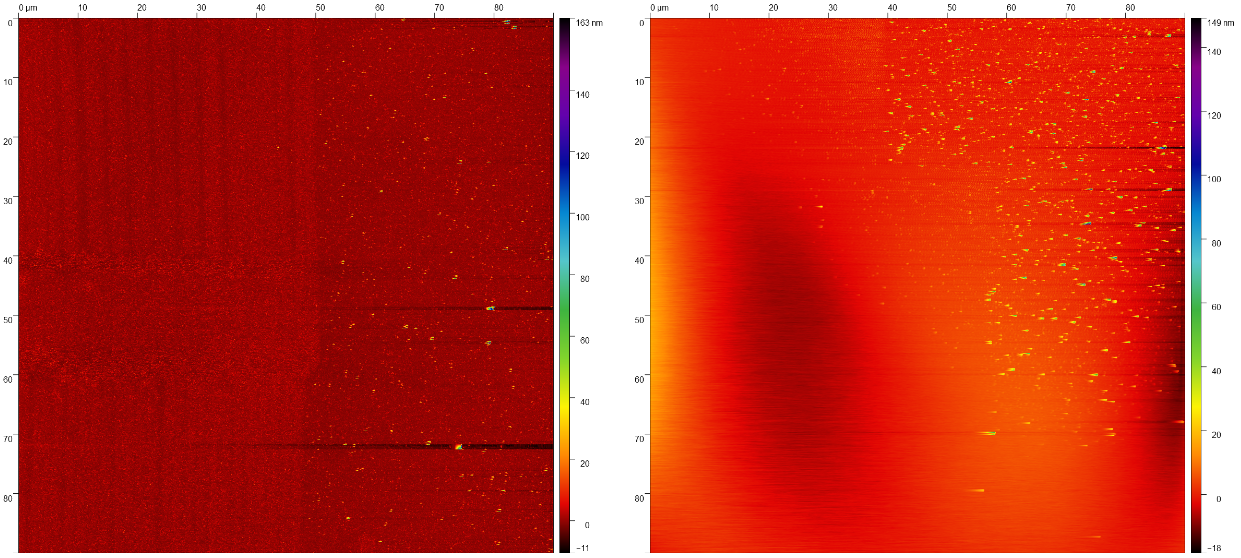

(a) spot 9

(b) spot 10

Figure 43: AFM height scan of Si-SiO_2-Si_yN_x sample at a) spot 9 and b) spot 10.

A.8 Fluences

Spot	**Fluence Si-Si$_y$N$_x$ ($\frac{J}{cm^2}$)**	**Fluence Si-SiO$_2$-Si$_y$N$_x$ ($\frac{J}{cm^2}$)**	**Fluence Si ($\frac{J}{cm^2}$)**
1	0.0036	0.0153	0.0070
2	0.0161	0.0208	0.0238
3	0.0530	0.0288	0.0491
4	0.1206	0.0375	0.1039
5	0.1590	0.0452	0.1671
6	0.2360	0.0649	0.2207
7	0.3447	0.0788	0.2426
8	0.4410	0.0989	0.2908
9	0.5877	0.1219	0.3500
10	0.6765	0.1349	0.3868
11	0.8563	0.1778	0.4701
12	1.1035	0.1909	0.5016
13	1.2885	0.2363	0.5804
14	1.3869	0.2728	0.6618
15	1.7097	0.2999	0.6671
16	1.9132	0.3381	0.8378
17	2.1306	0.3967	0.9826
18	2.3241	0.4275	0.9238
19	2.4780	0.4685	1.0964
20	2.7312	0.5495	1.1698
21	3.0539	0.5655	1.1908
22	3.3959	0.6416	1.2136
23	3.4312	0.6778	1.3196
24	3.5869	0.6680	1.5485
25	3.6655	0.7330	1.6109
26	3.6716	0.8061	1.3532
27	3.5088	0.8078	1.7927
28	3.7220	0.8976	1.7350
29	3.7332	0.9392	1.8037
30	3.7694	1.0003	2.0443
31	3.7826	1.0047	2.0802
32	3.7727	0.9755	2.1070
33	3.7846	1.0068	2.2729
34	3.7943	1.0429	2.1154
35	3.8097	1.0975	2.3494
36	3.7785	1.0885	2.3881

Table 4: Fluences for a single measurement grid of Si-Si$_y$N$_x$ 4, Si-SiO$_2$-Si$_y$N$_x$ 7 and Si.

B Acknowledgments

First and foremost, I would like to thank my daily supervisor Ester Abram for her amazing mentoring. I'm beyond grateful for her involvedness in the project and for incentivizing me to achieve the most. Her postive reinforcement whenever I made countless experimental mistakes, or her patience when I asked a myriad of questions about Liu analysis or the code is genuinely appreciated. Additionally, she's helped tremendously with the project. Namely, she's responsible for; Si-Si$_y$N$_x$ growth and laser damage, code for Fresnel Transfer Materix, part of her code used for analyzing experimental data given to me, helping with SEM imaging, proof-reading this report. Thank you Ester.

I would also like to thank Paul Planken for giving great insight on experimental results, but above all else, for making me a better scientist. His advice when trying to interpret the data was invaluable, and his scepticism always made sure I looked over everything a second time with more care. Furthermore, he's provided some great lectures on non-linear optics and Two-Temperature-Model, as well as some (much needed) pointers on how to give scientific presentations.

I'd also like to thank Vina Farmarzi for her immense involvement in project. She's given many valuable suggestions on experimental problems encountered. I appreciate the support she's offered and the weekly lighthearted chats we've had.

I'd like to thank Cristoph Morscher for his immense support during the project. He's essentially acted as a 2_{nd} daily supervisor and given countless feedback on experimental and theoretical questions I encountered. I'm also grateful for teaching me how to operate the femtosecond laser.

I'd also like to thank Dries van Oosten and Marnix Christiaan Willem Vreugdenhil for helping me make sense of the possible ablation mechanisms involved.